The Astrophysical Journal, 823:101 (22pp), 2016 June 1 doi:10.3847/0004-637X/823/2/101

ACHIEVING CONSISTENT DOPPLER MEASUREMENTS FROM *SDO*/HMI VECTOR FIELD INVERSIONS

Peter W. Schuck[1], S. K. Antiochos[2], K. D. Leka[3], and Graham Barnes[3]
[1] Space Weather Laboratory, Code 674, Heliophysics Science Division, NASA Goddard Space Flight Center, 8800 Greenbelt Rd., Greenbelt, MD 20771, USA; peter.schuck@nasa.gov
[2] Heliophysics Science Division, NASA Goddard Space Flight Center, 8800 Greenbelt Rd., Greenbelt, MD 20771, USA; spiro.antiochos@nasa.gov
[3] NorthWest Research Associates, 3380 Mitchell Lane, Boulder, CO 80301, USA; leka@nwra.com, graham@nwra.com
Received 2015 November 19; accepted 2016 March 16; published 2016 May 26

ABSTRACT

NASA's *Solar Dynamics Observatory* is delivering vector magnetic field observations of the full solar disk with unprecedented temporal and spatial resolution; however, the satellite is in a highly inclined geosynchronous orbit. The relative spacecraft–Sun velocity varies by ± 3 km s^{-1} over a day, which introduces major orbital artifacts in the Helioseismic Magnetic Imager (HMI) data. We demonstrate that the orbital artifacts contaminate all spatial and temporal scales in the data. We describe a newly developed three-stage procedure for mitigating these artifacts in the Doppler data obtained from the Milne–Eddington inversions in the HMI pipeline. The procedure ultimately uses 32 velocity-dependent coefficients to adjust 10 million pixels—a remarkably sparse correction model given the complexity of the orbital artifacts. This procedure was applied to full-disk images of AR 11084 to produce consistent Dopplergrams. The data adjustments reduce the power in the orbital artifacts by 31 dB. Furthermore, we analyze in detail the corrected images and show that our procedure greatly improves the temporal and spectral properties of the data without adding any new artifacts. We conclude that this new procedure makes a dramatic improvement in the consistency of the HMI data and in its usefulness for precision scientific studies.

Key words: instrumentation: polarimeters – methods: data analysis – Sun: granulation – Sun: helioseismology – Sun: magnetic fields

1. INTRODUCTION

The Helioseismic Magnetic Imager (HMI) aboard NASA's *Solar Dynamics Observatory* (*SDO*) produces full-Sun vector magnetic field observations at $1''$ resolution with a cadence of approximately 12 minutes. These data represent an unprecedented opportunity to study time evolution of solar vector magnetic fields on the spatial scales and timescales of active region evolution. For the first time relatively pristine data are available that are uncontaminated by the effects of Earth's atmospheric turbulence, which causes distortions that often cannot be completely corrected by speckle reconstruction imaging or adaptive optics. In principle, the HMI data can lead to major advances in science understanding, because the energy and helicity transported through the photosphere and into the corona can be determined by measuring plasma velocities (optical flow/image motions) from a sequence of photospheric vector magnetograms (Schuck 2005, 2006, 2008) where extrapolation methods are likely to fail (De Rosa et al. 2009; Peter et al. 2015). While speckle reconstruction imaging and adaptive optics can dramatically improve the local resolution of the images, these techniques often do not preserve the relative distances between solar structures from frame to frame, which introduces large artificial biases in velocity estimates. In contrast, *SDO* represents a stable platform with a known pointing, located outside Earth's atmosphere, thereby potentially permitting highly accurate measurements of the velocities between photospheric features from frame to frame.

SDO, however, is in a highly inclined geosynchronous orbit chosen so as to maximize data throughput to the ground-based receiving stations. Unfortunately, this orbit produces a large ± 3 km s^{-1} variation in the relative velocity between the HMI instrument and the Sun, which leads to major orbital artifacts in the HMI data. Since the orbit is accurately known, it would seem that removal of the artifacts should be straightforward, but even after five years into the mission, the exact mechanisms that contaminate the data remain a mystery and the rigorous removal of the artifacts has not been accomplished. There is speculation that the artifacts are caused by low spectral resolution combined with the motion of the Fe I $\lambda_0 = 6173.343$ Å line across the HMI transmission filters as the satellite executes its geosynchronous orbit. Given that *SDO*/HMI typically produces *I, Q, U,* and *V* images sampled at six wavelengths, the 24 data points at each pixel are already near critical sampling—marginally enough data to determine eight observables via Milne–Eddington inversion.[4] Over the period of an orbit the radial velocity of the satellite varies by as much as ± 3.2 km s^{-1}, which corresponds to a shift of $\Delta\lambda \simeq \lambda_0\, 2\, \Delta v/c \simeq 131$ mÅ, which is almost twice the nominal HMI filter separation of $\Delta\lambda \simeq 69$ mÅ. Such a large shift in the line, combined with the low spectral sampling and known parameter degeneracies, seems sure to create (or exacerbate) vulnerabilities in the Milne–Eddington inversion (see p. 275 in Borrero et al. 2011 and also Section 3.2 in Centeno et al. 2014). Some of the other possible causes for the orbital artifacts that have been suggested include errors in the transmission profiles, distortion of the optics due to gravitational effects, and asymmetries in the line profiles.[5]

Nonetheless, it is now well established that these artifacts contaminate many observables computed from HMI data (e.g., Section 7.1 in Hoeksema et al. 2014; Figure 4 in Liu & Schuck [2012] for AR 11072 shows oscillations in the shear helicity flux, Figure 3 in Chintzoglou & Zhang [2013] exhibits clear dips in the magnetic field near midnight on February 14–16,

[4] There are 11 possible observables that can be determined via a Milne–Eddington inversion. However, for the "fd10" release of the HMI data used in this paper, the filling factor is constrained to be $\alpha = 1$, the damping parameter of the Voigt profile is constrained to be $a = 0.5$, and the macroturbulence parameter $v_{\rm mac}$ is set to a constant (Centeno et al. 2014).
[5] Asymmetries in the line profiles could be addressed with higher spectral sampling.

and the Poynting flux in Figure 2 of Vemareddy [2015] shows a very clear 12 hr oscillation). The optimal solution would be to understand the source of the contamination at the spectral level and correct optical distortions through calibration prior to any inversion process to estimate Doppler velocities and magnetic fields. However, even if the source of the contamination is definitively identified and corrected for future observations, it is not guaranteed that these corrections could be implemented for the data already archived. If the HMI data are to be used to quantitatively investigate the variations in solar photospheric plasma, or to reliably supply data-driven models, it is absolutely essential that a rigorous procedure be developed to mitigate nonphysical temporally varying artifacts from both the archived and future data.

In this paper we present a new approach, COADRED (Cleansing Orbital Artifacts—Demodulation by REnormalizing Data), for correcting the downstream Doppler velocities derived from the Milne–Eddington inversions. It should be emphasized that all spatial and temporal scales are affected by the artifacts, thereby severely limiting the usefulness of the data for detailed quantitative spatiotemporal analysis at the cadence of the data series such as for Poynting flux estimates (Kazachenko et al. 2015). The goal of our procedure described below is to provide a data set that is consistent, i.e., free of orbital artifacts, but not necessarily calibration errors. Note that we cannot claim to derive data that are absolutely correct, because there are no absolute calibrations for the measurements. Potentially intercalibration between vector magnetographs could determine which measurements are correct. However, even understanding the relative calibrations between magnetographs is rife with complexities, because magnetograms often use different magnetically sensitive lines corresponding to different heights in the solar atmosphere, with different spatial resolutions, different spectral sampling, and different time cadence (Wang et al. 1992; LaBonte et al. 1999; Orozco Suárez et al. 2007; Leka et al. 2009; Leka 2011; Leka & Barnes 2012; Liu et al. 2012; Hoeksema et al. 2014). Given these many obstacles to determining absolute calibrations for the purposes of "correcting" any of the observables from the HMI pipeline data, we focus our attention instead on producing *consistent* data by renormalizing the observables to the radial rest velocity of the satellite with respect to the Sun: $V_R \rightarrow 0$. We emphasize that even the measurements observed at $V_R = 0$ may not be "correct" in an absolute sense. Indeed, we will show that significant biases remain in both large-scale flows and a small-scale Fresnel pattern. However, this renormalization does remove most of the contamination correlated with the spacecraft radial velocity. The result is consistent Doppler measurements that can now be used for spatiotemporal analysis of the image dynamics.

1.1. The COADRED Procedure

COADRED consists of a three-stage process for obtaining consistent Doppler measurements[6] with vector field data from the HMI pipeline.

1. The first step is to remove the projection of the satellite velocity along the line of sight (LOS) from each pixel. Since the satellite orbit is known with high accuracy, then in principle, if the HMI measurements were accurate, there would be no orbital effects remaining in the data. As will be shown below, however, this is definitely not the case.
2. We next remove the three well-known quasi-steady-state signals from each image: the differential rotation, the meridional flows, and the convective blueshift. Note that the first two are actual physical flows but the latter is not. As discussed in detail by Beckers & Nelson (1978), the convective blueshift, commonly referred to as the limb shift, is due to the observed strong correlation in photospheric lines between intensity and wavelength shift. For unresolved convective flows this correlation introduces a systematic bias to any line shift determinations, and this bias has a strong center-to-limb variation. The three large-scale signals are removed by fitting each image with a series of eigenfunctions representing the differential rotation, the meridional flows, and the limb shift "flows" and subtracting these from each image. Not surprisingly, these biases vary with *SDO*'s radial velocity V_R, and thus by removing them from each image, we reduce the power in the orbital effects substantially. We find that a low-order (∼8) series for each type of flow is sufficient for fitting and removing the large-scale biases. By determining the dependence of these coefficients on radial velocity, they may be projected to the same velocity, arbitrarily chosen to be the radial rest velocity of the *SDO* $V_R \equiv 0$, by interpolation.
3. After removal of these biases, we expect that the only remaining physical effects in the residual images are the small-scale convective dynamics, which should be largely quasi-stationary. However, we show below that these residual images still exhibit substantial orbital artifacts. We conjecture that these artifacts are caused by some type of interference between the instrument response and convective structures moving across the solar disk, which produces spectral artifacts by spatiotemporal modulation of the convective amplitudes. If so, then we expect there to be a strong correlation of *SDO*'s radial velocity with the limb shift effect in the instrument response. To remove this artifact, we calculate the magnitude of each residual image and then fit this with an eighth-order series of limb shift eigenfunctions. This yields the dependence of the coefficients on the satellite radial velocity V_R. As will be shown below, these coefficients also exhibit a clear systematic dependence with V_R, which must be due to orbital artifacts. Similar to the second step, we simply renormalize each pixel so that each image appears to be observed at the same radial velocity, again *arbitrarily* but consistently chosen to be $V_R \equiv 0$. This renormalization almost completely eliminates the remaining orbital signal. Corrected Dopplergrams are then constructed by restoring the large-scale flows, interpolated to $V_R = 0$, to the renormalized convection images to obtain HMI Dopplergrams that exhibit essentially no orbital artifacts and that now can be used for accurate science investigations. This procedure does not remove the steady-state biases in the Dopplergrams present at $V_R = 0$ such as the bias in the large-scale meridional flows described in Section 3.2.4 or the small-scale Fresnel pattern described in Section 4.

In the sections below we describe the data set that we used for this analysis and describe exactly how the COADRED

[6] Specifically the hmi.ME_720s_fd10{vlos_mag} data.

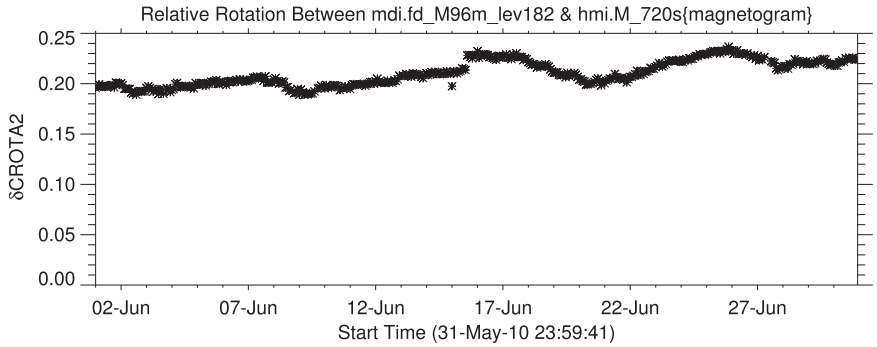

Figure 1. Relative roll angle between HMI Camera #1 and MDI based on the hmi.M_720s series.

procedure was applied to this data set. The procedure ultimately uses 32 velocity-dependent coefficients to adjust 10 million pixels—a remarkably sparse correction model given the complexity of the orbital artifacts. The data and the procedure are described in sufficient detail that others can use our methods or can modify them for application to other types of data sets.

2. DATA DESCRIPTION

Approximately 17 days of *SDO*/HMI data in 2010 are considered in developing the COADRED procedure. During this time period, the Sun was fairly quiet, but these days encompass the disk passage of the small and nearly potential active region AR 11072 discussed by Liu & Schuck (2012). This time period was specifically chosen for two reasons. First, it was a relatively quiet period, and therefore most pixels represented the same physical process of solar convection. This permitted the straightforward disentanglement of the orbital effects and the physical solar effects. Second, there was coverage by both HMI and MDI during this time.

The HMI has two independent cameras that produce several data series, which undergo different analysis. Consequently, these data sets may be used to intercompare observations of the Sun. Three data series are produced by the vector field "side camera" (Keyword CAMERA = 1). The hmi.M_720s{Magnetogram} and hmi.V_720s{Dopplergram} series are produced by an MDI-like algorithm (Couvidat et al. 2012) and the hmi.ME_720s_fd10 series with segments {field, azimuth, inclination, vlos_mag, etc.} (Hoeksema et al. 2014), which are produced by the Very Fast Inversion of the Stokes Vector (VFISV; Borrero et al. 2011; Centeno et al. 2014) Milne–Eddington code. Two data series are produced by the Doppler camera (Keyword CAMERA = 2) hmi.M_45s{Magnetogram} and hmi.V_45s{Dopplergram} (Scherrer et al. 2012; Schou et al. 2012; Hoeksema et al. 2014). The magnetogram and Dopplergram series have corrections and calibrations that are not applied to the spectral data provided to the Mile-Eddington inversions that are part of the hmi.ME_720s_fd10 series (Hoeksema et al. 2014). Furthermore, during 2010 there was a significant period of overlap in the observing programs of HMI and MDI. The MDI instrument produces two series that are comparable to observables estimated by HMI, namely, mdi.fd_M_96m_lev182, which is a LOS magnetogram, and mdi.fd_V, which is a LOS Dopplergram. Thus, in principle, there are three independent cameras and four different data sets for each LOS observable available for intercomparison for AR 11084. This paper will focus on the hmi.ME_720s_fd10{vlos_mag} data from the vector field "side camera," which measures 4096 x 4096 filtergrams at six wavelengths and four polarizations of the Fe I 617.3 nm line that are corrected for solar rotation, cosmic rays, distortions, and other effects (Hoeksema et al. 2014). These spectral data are used to construct the Stokes parameters (*I, Q, U, V*), which are in turn inverted based on the Milne–Eddington approximations using VFISV to produce about 8 physical parameters (see footnote 4), including the magnetic components relative to the LOS $\boldsymbol{B}_\xi$, $\boldsymbol{B}_\eta$, $\boldsymbol{B}_\zeta$ and the magnetized plasma velocity along the LOS $v_{\rm LOS}$. Since the data are spectrally sparse and the Milne–Eddington model is a simplified description of the line-forming physics, the inversion of these spectra is highly sensitive to the relative velocity between the instrument and the line-forming region on the Sun.

2.1. Camera #1 Orientation

The pointing of HMI is known to very high accuracy owing to the Venus transit data of 2012 June 5–6 (Couvidat 2014; Emilio et al. 2015). In particular, The CROTA2 keyword is often taken to be the orientation of the Sun's north pole in solar images. However, this interpretation depends specifically on how CROTA2 is determined. For HMI, the CROTA2 keywords are known to better than $0\overset{\circ}{.}002$ (Couvidat 2014) *relative to the transit of Venus*. We caution the reader that this is not an absolute determination relative to the Sun's north pole relative to either magnetic phenomena or solar flows. Furthermore, the P-angle and B0-angle estimates in the HMI pipeline keywords do not include the corrections to the Carrington elements determined by Beck & Giles (2005) using time–distance helioseismology on data from *SOHO*/MDI. Beck & Giles (2005) found that Carrington's estimates of i, the angle between the plane of the ecliptic and the solar equator, and Ω, the angle between the cross point of the solar equator with the ecliptic and the vernal equinox, were off by as much as $\Delta i = 0.095 \pm 0\overset{\circ}{.}002$ and $\Delta\Omega = -0.17 \pm 0\overset{\circ}{.}1$, with the error in i affecting the error in P-angle and CROTA2 more than the error in Ω. This may introduce a temporal error in CROTA2 of as much as $0\overset{\circ}{.}1$ depending on the heliocentric ecliptic longitude of the *SDO*. Furthermore, Beck & Giles (2005) concluded that the cross-equatorial flow they measured could correspond to a systematic bias in P-angle of another $\simeq 0\overset{\circ}{.}1$ under the assumption that the Sun does not maintain long-term cross-equatorial flows. These results suggest that generally there may be a time-dependent error in the inferred direction of solar north of as much as $\simeq 0\overset{\circ}{.}2$–$0\overset{\circ}{.}3$ when using the standard Carrington elements (this is not an HMI specific statement). Knowing these systematics is important for interpreting meridional flows, as we shall see in Section 3.2.

Figure 1 shows the relative angle between HMI Camera #1 and MDI based on the normalized cross-correlation of the mdi.fd_M_96m_lev182 and the hmi.M_720s series during 2010 June. The MDI series keywords CRVAL1 and CRVAL2 were adjusted by 1.9 and −0.5, respectively, to maximize the cross-correlation coefficient $C \simeq 0.9$ for the results presented here. The MDI image was convolved with a Gaussian filter, $\sigma_{\rm MDI} = 1$ pixel, and the HMI image was convolved with $\sigma_{\rm HMI} = 4 \times 0.875 = 3.5$ pixels, chosen to maximize the cross-correlation. Convolving both data sets with a Gaussian reduces shot noise. The CROTA2 value for the HMI image was then adjusted by CROTA2 → CROTA2 − δCROTA2 over a range of -1° to 1° where positive δCROTA2 corresponds to a counterclockwise (clockwise) rotation of HMI (MDI) to bring them into alignment. The Carrington/Stonyhurst coordinates (see Appendix B) were used to determine the same locations on each image, and the blurred HMI image was resampled to MDI observations. The offset between the two cameras lies between $0\overset{\circ}{.}18$ and $0\overset{\circ}{.}23$. The variation could be due to a drift in CRPIX or roll in MDI. At present, there is no predictive or definitive attitude data for *SOHO* during this time period.[7] However, these values are in rough agreement with Liu et al. (2012), who found $\delta{\rm CROTA2} \simeq 0.22 - 0.10 = 0\overset{\circ}{.}12 \pm 0\overset{\circ}{.}05$ in a comparison between the same two data series using a slightly different procedure and similar to the estimate $\delta{\rm CROTA2} \simeq 0.21$ for the offset between MDI and the Carrington elements determined from Doppler images (Hathaway & Rightmire 2010). These results imply that a CROTA2 value of 180 for HMI camera#1 corresponds closely to solar north pointing downward in the images to within a few tenths of a degree. This close alignment between HMI and MDI suggests that the large cross-equatorial flow implied by the S_1^0 coefficient determined in Section 3.2.3 is caused by instrument bias, not a misalignment in the camera orientation during this time period.

2.2. Co-registration

Owing to the orbit of *SDO*, the diameter (radius) of the Sun in HMI images varies by roughly 1″ (0.″5), corresponding to roughly 2 pixels on the timescale of a day, and on the timescale of 17 days the diameter (radius) of the Sun varies by roughly 2″ (1″), corresponding to roughly 4 (2) pixels. For spatiotemporal analysis, the optimal solution would be to track the active region across the Sun at the average speed of the active region. However, nonuniformities in the HMI instrument response then convolve noise in space and time. The co-registration choice for the remainder of this investigation is to (1) shift each image so that the center of the Sun corresponds to the center of the image (CRPIX1 = 2048.5, CRPIX2 = 2048.5), (2) rotate each image to the same orientation (CROTA2 = 0), and (3) remap each image to the same observation point DSUN_OBS = 152017949201 m (distance to the Sun), so that the solar radius remains constant in pixel units. Using this co-registration convention, each pixel corresponds to the same nominal location on the solar disk.

3. DOPPLER DATA PROCESSING

The following sections describe the procedure by which the HMI data are processed in order to remove the orbital artifacts. In the subsequent analysis the variable U is used to represent components of a velocity on the surface of the Sun, and the variable $\boldsymbol{V}_{SDO}$ is used the spacecraft velocity, but generally $\mathcal{V}$ is used to represent a theoretical model of the LOS Doppler velocity and $v_{\rm LOS}$ is used to represent various stages of data processing $v_{\rm LOS-0}$, $v_{\rm LOS-1}$, $v_{\rm LOS-2}$, and $v_{\rm LOS-3}$, with $v_{\rm LOS-0}$ representing the raw observed Doppler velocity from the HMI pipeline. The coordinate systems used are described in the Appendices based on the notation in Thompson (2006). In particular, Appendix B describes the projection of the Stonyhurst unit vector $(\widehat{\boldsymbol{\Phi}}, \widehat{\boldsymbol{\Theta}}, \hat{\boldsymbol{r}})$ onto the LOS.

3.1. Stage 1: Subtraction of the LOS Projection of Satellite Velocity

The first stage in the analysis is the removal of the LOS projection of the satellite velocity (Sat-V) from each pixel. The heliocentric Cartesian LOS direction $(\hat{\boldsymbol{x}}, \hat{\boldsymbol{y}}, \hat{\boldsymbol{z}})$ in helioprojective coordinates (θ_ρ, ψ) is (see Appendix A)

$$\hat{\boldsymbol{\eta}}_{\rm LOS}(\theta_\rho, \psi) = \sin\theta_\rho \sin\psi\, \hat{\boldsymbol{x}} - \sin\theta_\rho \cos\psi\, \hat{\boldsymbol{y}} + \cos\theta_\rho\, \hat{\boldsymbol{z}}. \tag{1}$$

Positive values of Doppler shift correspond to (redshifts) motion away from the satellite.[8] In principle, the LOS plasma motion on the Sun can be determined by subtracting the projection of the satellite motion onto the LOS from the measured Doppler velocity at each pixel i,

$$v_{{\rm LOS}-1,i} = v_{{\rm LOS}-0,i} - \hat{\boldsymbol{\eta}}_{\rm LOS} \cdot \boldsymbol{V}_{SDO} \equiv -\hat{\boldsymbol{\eta}}_{\rm LOS} \cdot \boldsymbol{U}_{\rm surface}. \tag{2}$$

The velocity vector for *SDO* in the heliocentric Cartesian directions is

$$\boldsymbol{V}_{SDO} = (V_{\rm W}, V_{\rm N}, V_{\rm R}) \tag{3a}$$

$$= ({\rm OBS\_VW}, {\rm OBS\_VN}, {\rm OBS\_VR}), \tag{3b}$$

in the heliographic Cartesian coordinate system, and thus

$$\hat{\boldsymbol{\eta}}_{\rm LOS} \cdot \boldsymbol{V}_{SDO} = {\rm OBS\_VW} \sin\theta_\rho \sin\psi - {\rm OBS\_VN} \sin\theta_\rho \cos\psi + {\rm OBS\_VR} \cos\theta_\rho. \tag{4}$$

Here $V_{\rm R}$ corresponds to the HMI keyword "OBS_VR," which is the velocity of the observer in the solar-radial direction (positive is away from Sun). Additionally, $V_{\rm W}$ corresponds to the HMI keyword "OBS_VW," which is the velocity of the observer solar-westward (positive in the rough direction of Earth's orbit), and $V_{\rm N}$ corresponds to "OBS_VN," which is the velocity of the observer solar-northward (positive in the direction of solar north).

If the Doppler velocities are measured accurately, the $v_{\rm LOS-1}$ would show no correlation with satellite motion. The black line in Figure 2 shows the residual spatially averaged rms Doppler velocity

$$\text{Residual} = \langle \Delta \boldsymbol{v}_{\rm LOS}^2 \rangle_x - \langle \Delta \boldsymbol{v}_{\rm LOS}^2 \rangle_{x,t}, \tag{5}$$

during 17 days in 2010 after the projection of the satellite velocity has been subtracted from each pixel via Equation (2). The subscripts "x" and "t" indicate spatial and temporal averaging, respectively. A large, daily oscillation remains, indicating *systematic* errors in the LOS Doppler measurements from the vector field inversions. Similar oscillations are known to occur in the B from the vector field inversions (see Hoeksema et al. 2014)

[7] http://sohowww.nascom.nasa.gov/data/ancillary/#attitude

[8] http://jsoc.stanford.edu/doc/data/hmi/sharp/old/sharp.MB.htm

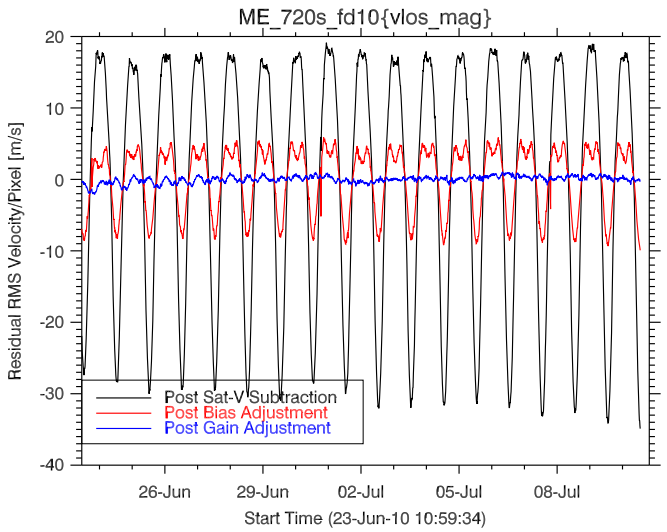

Figure 2. Residual spatially averaged rms Doppler velocity during 17 days in 2010. Black: after the projection of the satellite velocity has been removed from each pixel. Red: after solar rotation $V_{\rm Rot}$, meridional flows $V_{\rm MF}$, and limb shift $V_{\rm LS}$ have been removed. See Sections 3.1, 3.2.4, and 3.4 for a description of the black, red, and blue curves, respectively.

and in the hmi.V_720s{Dopplergram} series from the same camera and in the 45 s cadence data from the hmi.V_45s series observed by camera 2 (private communication with Phil Scherrer). This strong fixed oscillation convolves with and contaminates all spatial and temporal scales, which greatly diminishes the usefulness of the data for science studies.

3.2. Stage 2: Large-scale Biases

The second stage in the COADRED procedure is the decomposition of each Doppler image into large-scale flows: differential rotation flows $\mathcal{V}_{\rm MF}$, meridional flows $\mathcal{V}_{\rm MF}$, and the convective blueshift (limb shift) component $\mathcal{V}_{\rm LS}$. This determines an effective "bias" for each image according to

$$\mathcal{V}_{\rm bias} = \mathcal{V}_{\rm Rot}(B_0, \Phi, \Theta) + \mathcal{V}'_{\rm LS}(\varrho) + \mathcal{V}'_{\rm MF}(B_0, \Phi, \Theta), \quad (6)$$

where Φ and Θ are the Stonyhurst coordinates (Thompson 2006), B_0 is the so-called Solar-B angle, and ϱ is the heliocentric angle between the observer and the observed point (see Appendix C). The form of Equations (4) and (2) suggests that artifacts introduced by the observer's radial velocity will project onto the limb shift functions (cylindrical symmetry), artifacts introduced by the observer's westward velocity will project onto the differential rotation profile, and artifacts introduced by the observer's northward velocity will project onto the meridional flow profile. Because the geosynchronous orbit of *SDO* causes significant changes in the radial velocity $V_{\rm R}$ over the period of a day, we conjecture that the projection of the radial velocity onto the limb shift functions is the most significant source of orbital artifacts in Dopplergrams. Consequently, step 3 of the procedure consists of a model for removing this effect, but first we must determine and subtract the known biases from each image. The following three sections describe the standard mathematical formulation for capturing the differential rotation, meridional flow, and limb shift "velocity." We then discuss, in detail, our application of this formalism to the HMI data.

3.2.1. Rotational Velocity

Following Hathaway (1988), the solar differential rotational velocity is decomposed by

$$U^0_\Phi(\Theta) = \sum_{\ell=1}^{\ell_{\rm max}} T^0_\ell \sqrt{\ell(\ell+1)}\, \overline{P}^1_\ell(\sin\Theta), \quad (7)$$

where

$$\overline{P}^m_\ell(x) \equiv (-1)^m \sqrt{\frac{(2\ell+1)(\ell-m)!}{2(\ell+m)!}}\, P^m_\ell(x), \quad (8)$$

and where P^m_ℓ are the associated Legendre functions[9]

$$\int_{-1}^{1} dx\, P^m_k(x) P^m_\ell(x) = \frac{2(\ell+m)!}{(2\ell+1)(\ell-m)!}\, \delta_{k,\ell}. \quad (9)$$

Note that Equation (8) leads to the definition of the spherical harmonics,

$$Y^m_\ell(\theta, \phi) = (-1)^m \sqrt{\frac{(2\ell+1)}{4\pi}\frac{(\ell-m)!}{(\ell+m)!}}\, P^m_\ell(\cos\theta) e^{i\,m\,\phi} \equiv \overline{P}^m_\ell(\cos\theta)\frac{e^{i\,m\,\phi}}{\sqrt{2\,\pi}}. \quad (10)$$

Using Equation (1), the projection of this solar differential rotation velocity onto the LOS velocity is then

$$\mathcal{V}_{\rm Rot}(B_0, \Phi, \Theta) = -\hat{\eta}_{\rm LOS} \cdot \mathcal{J}^{\rm T} \cdot \widehat{\mathbf{\Phi}}\, U^0_\Phi(\Theta) \quad (11a)$$

where for $\theta_\rho \approx 0$ (see Appendix B)

$$\hat{\eta}_{\rm LOS} \cdot \mathcal{J}^{\rm T} \cdot \widehat{\mathbf{\Phi}} \approx -\cos B_0 \sin\Phi. \quad (11b)$$

The coefficients T^0_ℓ are related to the usual A, B, C coefficients in

$$\omega(\Theta) = A + B\sin^2\Theta + C\sin^4\Theta = \frac{1}{R_\odot \cos\Theta} \times \sum_{\ell=1}^{\ell_{\rm max}} T^0_\ell \sqrt{\ell(\ell+1)}\, \overline{P}^1_\ell(\sin\Theta) \quad (12)$$

by

$$A = \frac{1}{16}(8\sqrt{6}\, T^0_1 - 12\sqrt{14}\, T^0_3 + 15\sqrt{22}\, T^0_5), \quad (13a)$$

$$B = \frac{15}{8}(2\sqrt{14}\, T^0_3 - 7\sqrt{22}\, T^0_5), \quad (13b)$$

$$C = \frac{315}{8}\sqrt{\frac{11}{2}}\, T^0_5. \quad (13c)$$

where $R_\odot = 695,946 \pm 15$ km is the radius of the Sun for HMI (Emilio et al. 2015).

3.2.2. Limb Shift Velocity

Following Snodgrass (1984) and Hathaway (1992, 1996), the convective blueshift, caused by correlations between velocity and intensity in unresolved convective elements

[9] As in Mathematica® and Interactive Data Language (IDL)®.

(Beckers & Nelson 1978), is decomposed as

$$\mathcal{V}'_{\rm LS}(\varrho) = \sum_{\ell=0}^{N_{\rm LS}} L_\ell (2\ell+1)^{-1/2}\, \mathcal{L}_\ell(1-\cos\varrho), \tag{14a}$$

where ϱ is the heliocentric angle between the observer and the observed point as defined in Appendix C, and

$$\mathcal{L}_\ell(x) = \sqrt{2}\, \overline{P}^0_\ell(2\,x-1) \tag{14b}$$

are shifted Legendre polynomials orthonormal on (0, 1). A prime is used in Equation (14a) to indicate that this is an adjusted limb shift function, for reasons that will become apparent below.

3.2.3. Meridional Velocity

Again, following Hathaway (1992, 1996), the meridional flows are decomposed as

$$U^0_\Theta(\Theta) = \sum_{\ell=1}^{\ell_{\rm max}} S^0_\ell \sqrt{\ell(\ell+1)}\, \overline{P}^1_\ell(\sin\Theta), \tag{15}$$

where positive coefficients correspond to northward velocities. In principle, the projection of the meridional flows is given by

$$\mathcal{V}_{\rm MF}(B_0, \Phi, \Theta) = -\hat{\boldsymbol{\eta}}_{\rm LOS}\cdot\boldsymbol{\mathcal{J}}^{\rm T}\cdot\widehat{\boldsymbol{\Theta}}\, U^0_\Theta(\Theta), \tag{16a}$$

where for $\theta_\rho \approx 0$ (see Appendix B)

$$\hat{\boldsymbol{\eta}}_{\rm LOS}\cdot\boldsymbol{\mathcal{J}}^{\rm T}\cdot\widehat{\boldsymbol{\Theta}} \approx \sin B_0\cos\Theta - \cos B_0\cos\Phi\sin\Theta. \tag{16b}$$

However, Hathaway (1988) noticed that the meridional flow given by Equation (15) has a projection onto the limb shift eigenfunctions. The limb shift eigenfunctions are described in heliocentric spherical eigenfunctions (see Appendix C), whereas the meridonal flows are described in LOS projected spherical eigenfunctions, where every ℓ, $m = 0$ will project onto the limb shift eigenfunctions. Thus, to orthogonalize the description of the large-scale flows, this projection must be subtracted from the meridional flow eigenfunctions as it has already been accounted for in the limb shift eigenfunctions. Thus, the actual meridional flow description used to fit each image at stage 1 is given by

$$\mathcal{V}'_{\rm MF}(B_0, \Phi, \Theta) = -\sum_{\ell=1}^{\ell_{\rm max}} S^0_\ell \sqrt{\ell(\ell+1)}\, [\hat{\boldsymbol{\eta}}_{\rm LOS}\cdot\boldsymbol{\mathcal{J}}^{\rm T}\cdot\widehat{\boldsymbol{\Theta}}\,\overline{P}^1_\ell(\sin\Theta) - G_{{\rm MF},\ell}(B_0,\varrho)], \tag{17}$$

where

$$G_{{\rm MF},\ell}(B_0,\varrho) = \frac{1}{2\,\pi}\int_0^{2\,\pi} d\psi\, \hat{\boldsymbol{\eta}}_{\rm LOS}\cdot\boldsymbol{\mathcal{J}}^{\rm T}\cdot\widehat{\boldsymbol{\Theta}}\,\overline{P}^1_\ell(\sin\Theta) \tag{18}$$

represents the spatial part of the meridional eigenfunction that is independent of position angle ψ. Indeed, Equation (18) is proportional to the meridional eigenfunction averaged over the position angle ψ. The integral in Equation (18) requires some effort to evaluate. The results were stated first by Hathaway (1988) without proof. A general proof in closed form is presented in Appendix D. The eigenfunctions describing $\mathcal{V}'_{\rm LS}$ are nearly orthogonal to $\mathcal{V}'_{\rm MF}$.[10] Once the coefficients L_ℓ and S^0_ℓ are determined, the meridional flow may be reconstructed with Equation (15) and the limb shift function may be reconstructed with

$$\mathcal{V}_{\rm LS}(B_0,\varrho) = \sum_{\ell=0}^{N_{\rm LS}} [L_\ell(2\ell+1)^{-1/2}\,\mathcal{L}_\ell(1-\cos\varrho) + S^0_\ell\sqrt{\ell(\ell+1)}\, G_{{\rm MF},\ell}(B_0,\varrho)]. \tag{19}$$

Note that

$$\mathcal{V}_{\rm LS}(B_0,\varrho) + \mathcal{V}_{\rm MF}(B_0,\Phi,\Theta) = \mathcal{V}'_{\rm LS}(B_0,\varrho) + \mathcal{V}'_{\rm MF}(B_0,\Phi,\Theta). \tag{20}$$

3.2.4. Determination of the Bias

To determine the bias, each image is fit using the eigenfunctions described in Sections 3.2.1–3.2.3. Hathaway (1988, 1992, 1996) noted that strong magnetic fields can alter the convection pattern. He used an iterative procedure that first determines an estimate of the spectral coefficients and then replaces the Doppler estimates in pixels corresponding to strong magnetic fields with estimates consistent with these coefficients. The procedure repeats until there are no further significant changes in the spectral coefficients.

The present analysis diverges significantly from that previous work. The image at each stage of analysis is reformed into column vectors $\boldsymbol{V}_{\rm LOS-1},\ldots,\boldsymbol{V}_{\rm LOS-3}$ representing all of the $N_{\rm D}$ pixels located on the solar disk and $\boldsymbol{v}_{\rm LOS-1},\ldots,\boldsymbol{v}_{\rm LOS-3}$ representing just the $N_{\rm W}$ weak-field pixels corresponding to an absolute LOS magnetic field less than or equal to 10 G *and* minimal support (CONF_DISAMBIG < 60) as determined by "confidence" in the pixel assigned the disambiguation module of the vector pipeline (for a complete description of the CONF_DISAMBIG values see Appendix A.5 on p. 3523 in Hoeksema et al. 2014).[11] For the 17 days under consideration $N_{\rm W}$ represents about 84% of the solar disk. In the same manner, two matrices of eigenfunctions are constructed, $\mathbf{E}$ and $\mathbf{e}$, representing the $M = N_{\rm R} + N_{\rm LS} + N_{\rm MF}$ eigenfunctions used to determine the large-scale Doppler patterns, where $\mathbf{E}$, which is $N_{\rm D}\times M$, represents all of the $N_{\rm D}$ pixels located on the solar disk and $\mathbf{e}$, which is $N_{\rm W}\times M$, represents just the $N_{\rm W}$ weak-field pixels. The goal is to determine a set of spectral coefficients $\boldsymbol{b}$ from the $N_{\rm W}$ stage 1 Doppler estimates in column vector $\boldsymbol{v}_{\rm LOS-1}$. Obviously, with $N_{\rm W}\simeq 10^7$ and $M\simeq 24$ there is no solution to the overdetermined system

$$\mathbf{e}\boldsymbol{b} = \boldsymbol{v}_{\rm LOS-1},$$

$$\begin{bmatrix} e_{11} & \cdots & e_{1M} \\ \vdots & \cdots & \vdots \\ e_{N_{\rm W}1} & \cdots & e_{N_{\rm W}M} \end{bmatrix} \begin{bmatrix} T^0_1 \\ \vdots \\ T^0_{N_R} \\ L_0 \\ \vdots \\ L_{N_{\rm LS}-1} \\ S^0_1 \\ \vdots \\ S^0_{N_{\rm MF}} \end{bmatrix} = \begin{bmatrix} v_{\rm LOS-1,1} \\ v_{\rm LOS-1,2} \\ v_{\rm LOS-1,3} \\ \vdots \\ v_{{\rm LOS-1},N_{\rm W}} \end{bmatrix}, \tag{21}$$

[10] They are not exactly orthogonal because the observations on the disk are discrete, and for simplicity we have orthogonalized these functions using continuous representations. See discussion in Section 3.4 and Figure 3.

[11] Strong-field pixels correspond to absolute LOS magnetic field greater than 10 G *or* significant support (CONF_DISAMBIG $\geqslant$ 60).

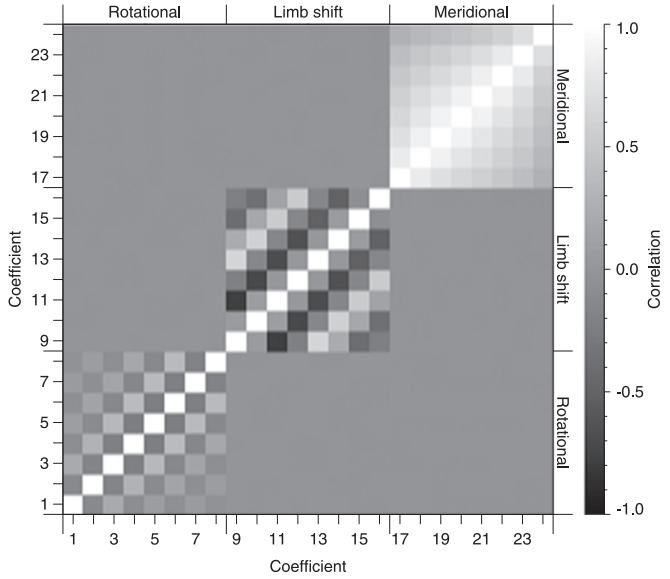

Figure 3. Correlations between the coefficients for the fit to the large-scale flows on 2010 July 04 at 17:00:00.

where $v_{\mathrm{LOS}-1,i}$ are the $i = 1,\ldots,N_{\mathrm{W}}$ stage 1 weak-field pixels determined from Equation (2) because no general inverse of the eigenvectors $\mathbf{e}$ exists. Instead, we attempt to find the solution that is best in an L_2 norm sense, where $\boldsymbol{b}^*$ minimizes

$$\|\mathbf{e}\boldsymbol{b}^* - \boldsymbol{v}_{\mathrm{LOS}-1}\|_2 \leqslant \|\mathbf{e}\boldsymbol{b} - \boldsymbol{v}_{\mathrm{LOS}-1}\|_2 \tag{22}$$

among all possible spectral coefficients $\boldsymbol{b}$. This optimal solution is determined directly from the least-squares solution

$$\boldsymbol{b}^* = (\mathbf{e}^{\mathrm{T}}\mathbf{e})^{-1}\mathbf{e}^{\mathrm{T}}\boldsymbol{v}_{\mathrm{LOS}-1}, \tag{23}$$

where $(\mathbf{e}^{\mathrm{T}}\mathbf{e})^{-1}\mathbf{e}^{\mathrm{T}}$ is known as the pseudo-inverse (Moore 1920; Bjerhammar 1951; Penrose 1955). Note that this approach explicitly ignores the strong-field pixels in determining the spectral coefficients circumventing the iterations necessary in Hathaway (1996).

The temporally varying bias image for each full-disk Dopplergram of N_{D} pixels can then be reconstructed from

$$\boldsymbol{B} = \mathbf{E}\boldsymbol{b}^*. \tag{24}$$

The large-scale bias-free stage 2 Dopplergrams are then determined from

$$\boldsymbol{V}_{\mathrm{LOS}-2} = \boldsymbol{V}_{\mathrm{LOS}-1} - \mathbf{E}\boldsymbol{b}^*. \tag{25}$$

Figure 3 shows the correlations between the $M = 24$ coefficients used to fit the large-scale Doppler patterns. The eigenfunctions are nearly block orthogonalized, e.g., there are correlations between the meridional eigenfunctions, but these eigenfunctions are nearly completely decoupled from the limb shift eigenfunctions, validating the corrections encompassed by Equations (17)–(20). Correlations within the block are expected as spherical harmonics themselves are not orthogonal on the observed solar hemisphere and they are further confused by the projection of the velocity component onto the LOS (Mochizuki 1992), the eigenfunctions are orthogonalized using a continuous representation rather than discrete sampling theorem, and some data locations are neglected because of significant magnetic fields. Note that the differential rotation eigenfunctions are for all practical purposes orthogonal to both the limb shift and merdional eigenfunctions by virtue of the former's antisymmetry across $\Phi = 0$ and the latter's symmetry across the same, even after the LOS projection is take into account.

Figures 4–6 show rotational, limb shift, and meridional spectral coefficients during 17 days in 2010 as determined from Equation (23). The black data are "high-quality" data, and the red data are "low-quality" data (Keyword: QUALITY $\neq 0$). We emphasize that since the satellite velocity has been removed from each pixel prior to fitting the Doppler data, there should be *no correlation* with the satellite velocity. However, clear, almost periodic oscillations are present with a primary period near 24 hr observed in the lowest spectral coefficients in all three figures. In Figure 4, the lowest coefficient exhibits a peak-to-peak amplitude 110 nrads s^{-1}or $\Delta v = \sqrt{2}\ \Delta T_1^0\ R_\odot \simeq 105\ \mathrm{m\ s}^{-1}$. Again, this indicates a significant error in the measurements, particularly near the limb, where solar rotation is the strongest in the LOS component. The blue line corresponds to the low-frequency trend, with a cutoff period of 48 hr determined from a nonparametric B-spline filter (Woltring 1986; Schuck 2010). The details of how this trend is determined are discussed in Section 3.4. The red curve in Figure 2 shows the residual spatially averaged rms Doppler velocity for the stage 2 Dopplergrams $\boldsymbol{V}_{\mathrm{LOS}-2}$. Removing the time-varying bias considerably improves the temporal stability of the Dopplergrams.

One of the most striking features of these results is the significant bias in the S_1^0 meridional coefficient exhibited in Figure 6. One explanation for this result is an average cross-equatorial flow of $\simeq -95\ \mathrm{m\ s}^{-1}$. A cross-equatorial flow of this magnitude would be easily detected by other techniques, so this explanation is ruled out. Another possible explanation for this bias is an error in position angle $\delta\psi = \tan^{-1}(S_1^0/A)$ in solar north, where A is determined from Equation (13*a*). A bias of $\simeq -95\ \mathrm{m\ s}^{-1}$ corresponds to error in position angle of about $2\overset{\circ}{.}6$. This explanation also seems incorrect given the agreement between the alignment of HMI and MDI magnetogram data exhibited in Figure 1. Therefore, our conclusion at present is that this bias in the S_1^0 coefficient represents a spatial nonuniformity in the response of HMI.

3.3. Stage 3: Gain Adjustment

The red curve in Figure 3 demonstrates that even after the known velocities are removed from the HMI data, there still remains a strong daily periodicity in the residual images, indicating contamination by orbital effects. Therefore, stage 3 of our COADRED procedure consists of a pixel-by-pixel, image-by-image adjustment of the gain. Given the strong, nearly periodic oscillations in the limb shift functions, we hypothesize that the gain of each pixel follows a similar pattern; consequently, we use the limb shift formalism to correct for this gain. Following the procedure in Section 3.2.4, two $\mathbb{R}^{N_{\mathrm{D}}\times N_{\mathrm{G}}}$ and $\mathbb{R}^{N_{\mathrm{W}}\times N_{\mathrm{G}}}$ matrices are constructed from the limb shift eigenfunctions, $\mathbf{E}_{\mathrm{LS}} = \mathbf{E}(1{:}\ N_{\mathrm{D}},\ N_{\mathrm{R}} + 1{:}\ N_{\mathrm{R}} + N_{\mathrm{LS}} + 1)$ and $\mathbf{e}_{\mathrm{LS}} = \mathbf{e}(1{:}\ N_{\mathrm{W}},\ N_{\mathrm{R}} + 1{:}\ N_{\mathrm{R}} + N_{\mathrm{LS}} + 1)$, corresponding to the $N_{\mathrm{G}} = N_{\mathrm{LS}}$ limb shift eigenfunctions used to fit the bias, where $\mathbf{E}_{\mathrm{LS}}$ represents all of the N_{D} pixels located on the solar disk and $\mathbf{e}_{\mathrm{LS}}$ represents just the N_{W} weak-field pixels. These eigenfunctions are then fit to the absolute value of the stage 2

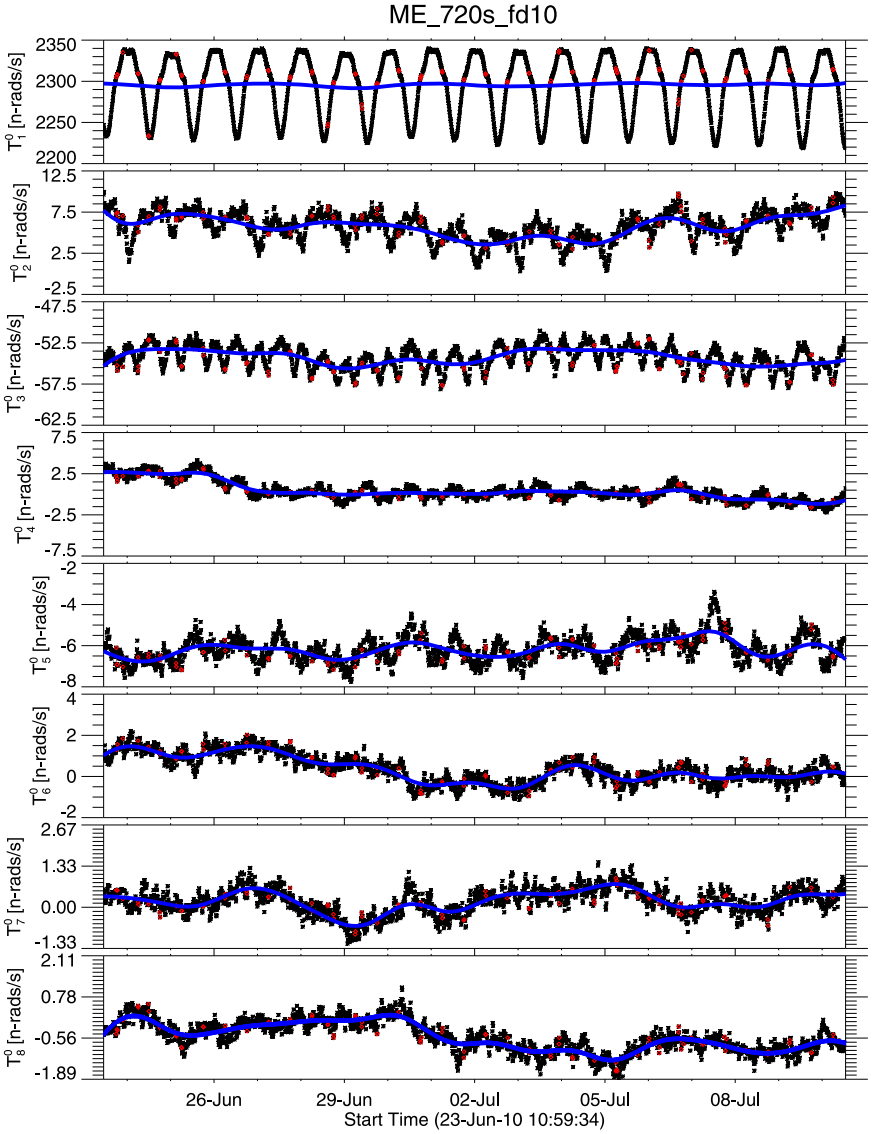

Figure 4. Rotational spectral coefficients during 17 days in 2010. The black data are "high-quality" data, and the red data are low-quality data (Keyword: QUALITY $\neq 0$). The blue line corresponds to the low-frequency trend determined after orbital artifacts are removed. See text for a complete discussion.

bias-subtracted Dopplergrams

$$\mathbf{e}_{\rm LS}\boldsymbol{g} = |\boldsymbol{v}_{\rm LOS-2}|,$$

$$\begin{bmatrix} e_{10} & \cdots & e_{1N_{\rm G}-1} \\ \vdots & \cdots & \vdots \\ e_{N_{\rm W}0} & \cdots & e_{N_{\rm W}N_{\rm G}-1} \end{bmatrix} \begin{bmatrix} g_0 \\ \vdots \\ g_{N_{\rm G}-1} \end{bmatrix} = \begin{bmatrix} |v_{\rm LOS-2,1}| \\ |v_{\rm LOS-2,2}| \\ \vdots \\ |v_{\rm LOS-2,N_W}| \end{bmatrix}, \quad (26)$$

which has the optimal least-squares solution

$$\boldsymbol{g}^* = (\mathbf{e}_{\rm LS}^{\rm T}\mathbf{e}_{\rm LS})^{-1}\mathbf{e}_{\rm LS}^{\rm T}\ |\boldsymbol{v}_{\rm LOS-2}|. \quad (27)$$

The gain for each image can then be reconstructed from

$$\boldsymbol{G} = \mathbf{E}_{\rm LS}\boldsymbol{g}^*. \quad (28)$$

Figure 7 shows the gain coefficients during 17 days in 2010 as determined from Equation (27).

3.4. Treatment of the Coefficients and Image Reconstruction

Plotting the data in Figures 4–7 as a function of $V_{\rm R}$ reveals their systematic *nonlinear* dependence on radial satellite velocity, as shown in Figures 8–11. The nonlinear response is the source of the almost periodic temporal dependence in the coefficients. The black data points in these figures are fit by weighted least squares with orthogonalized polynomials.[12] The weights for each data point are determined from the variance in the coefficients from the fits. The optimal polynomial order is determined using the Bayesian Information Criteria (Schwarz 1978; Ye et al. 2008)

$$\mathrm{BIC}_k \simeq N_{\rm D}\log\widehat{\sigma}^2_{\rm ML} + N_k\log N_{\rm D}, \quad (29)$$

where $N_{\rm D}$ is the number of data, N_k is the number of model parameters, and $\widehat{\sigma}^2_{\rm ML}$ is the maximum likelihood estimate of the variance. The optimal number of coefficients $k_{\rm opt}$ corresponds

[12] The red "low-quality" data are ignored.

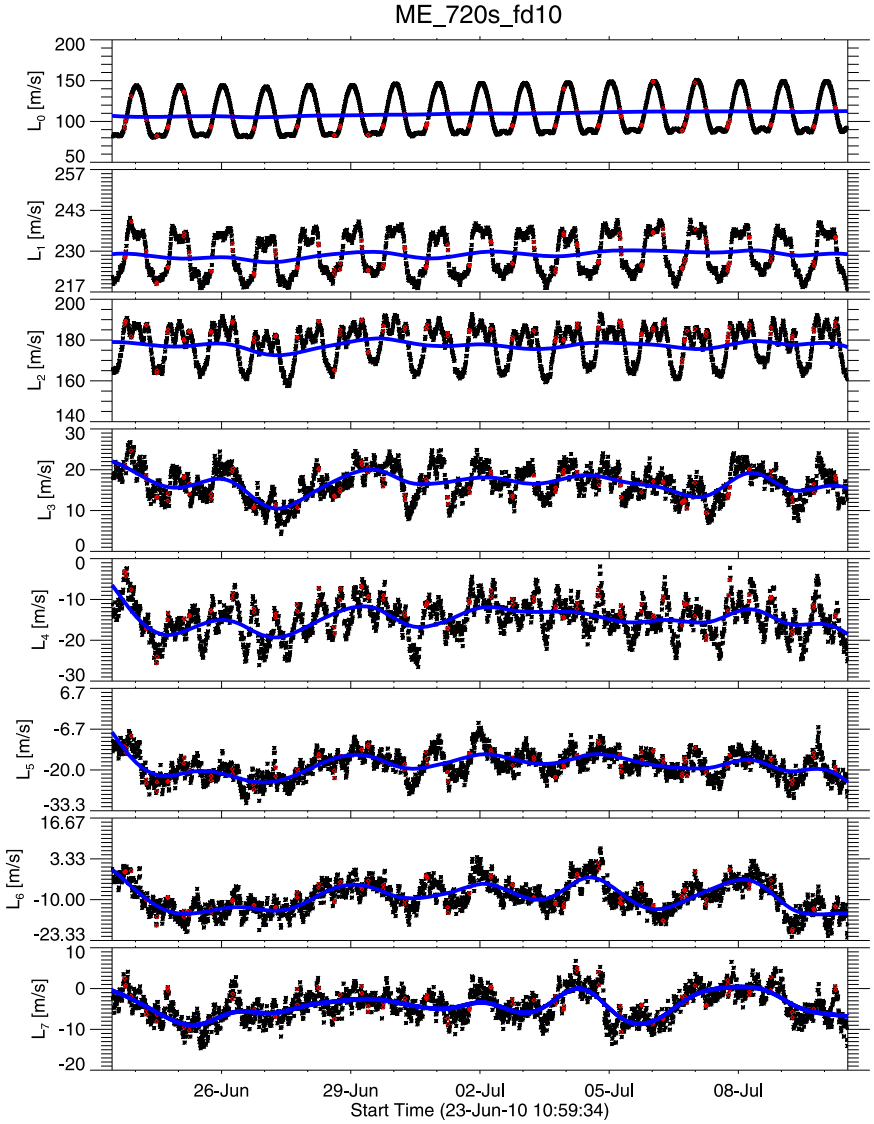

Figure 5. Limb shift spectral coefficients during 17 days in 2010. Same format as Figure 4.

to the model with the minimum BIC_k value.[13] We emphasize that the "model" involves two separate fitting processes: (1) the orthogonalized polynomial fit to the parameterized data in V_R space and (2) the temporal fit using a nonparametric B-spline filter to remove any systematic temporal drift in the parameters that would bias the orthogonalized polynomial fit. The B-spline filter has some attractive properties for this problem as data frames are occasionally missing and a B-spline filter can be interpreted as an optimal cascaded Butterworth filter generalized for unevenly sampled data (Craven & Wahba 1979). The number of degrees of freedom removed from the data by the smoothing procedure can be determined from the trace of the influence matrix of the B-spline filter (Wahba 1980; Woltring 1986). The maximum likelihood estimate of the error variance is computed from the residuals by subtracting both of these fits from the stage 1 data, and therefore N_k in Equation (29) must reflect both of these fitting processes, i.e., the order of the orthogonalized polynomial and the trace of the influence matrix of the B-spline filter. The smoothing parameter of the B-spline filter is fixed with a cutoff of 48 hr, and some iteration is necessary to minimize the BIC and find the optimal coefficients for each polynomial order k.

Using the low-frequency response and the orthogonalized polynomial fit corresponding to the blue and green curves in Figures 4–7, a model for the *predicted* bias and gain coefficients may be determined for any radial velocity V_{R} and time t in the data set

$$\beta(V_{\mathrm{R}}, t) = \beta_{\mathrm{LF}}(t) + \beta_{\mathrm{OP}}(V_{\mathrm{R}}), \tag{30a}$$

$$\gamma(V_{\mathrm{R}}, t) = \underbrace{\gamma_{\mathrm{LF}}(t)}_{\text{blue}} + \underbrace{\gamma_{\mathrm{OP}}(V_{\mathrm{R}})}_{\text{green}}. \tag{30b}$$

The stage 3 Dopplergrams are reconstructed by subtracting off the *observed* bias, dividing by the *observed* gain, and then multiplying by the *predicted* gain.

$$\boldsymbol{V}_{\mathrm{LOS}-3} = [\mathbf{E}_{\mathrm{LS}}\boldsymbol{\gamma}(0, t)] \oslash [\mathbf{E}_{\mathrm{LS}}\boldsymbol{g}^*] \odot [\boldsymbol{V}_{\mathrm{LOS}-1} - \mathbf{E}\boldsymbol{b}^*], \tag{30c}$$

[13] The application of BIC does not require that the true model is in the set of models (polynomials) under consideration (Cavanaugh 1999).

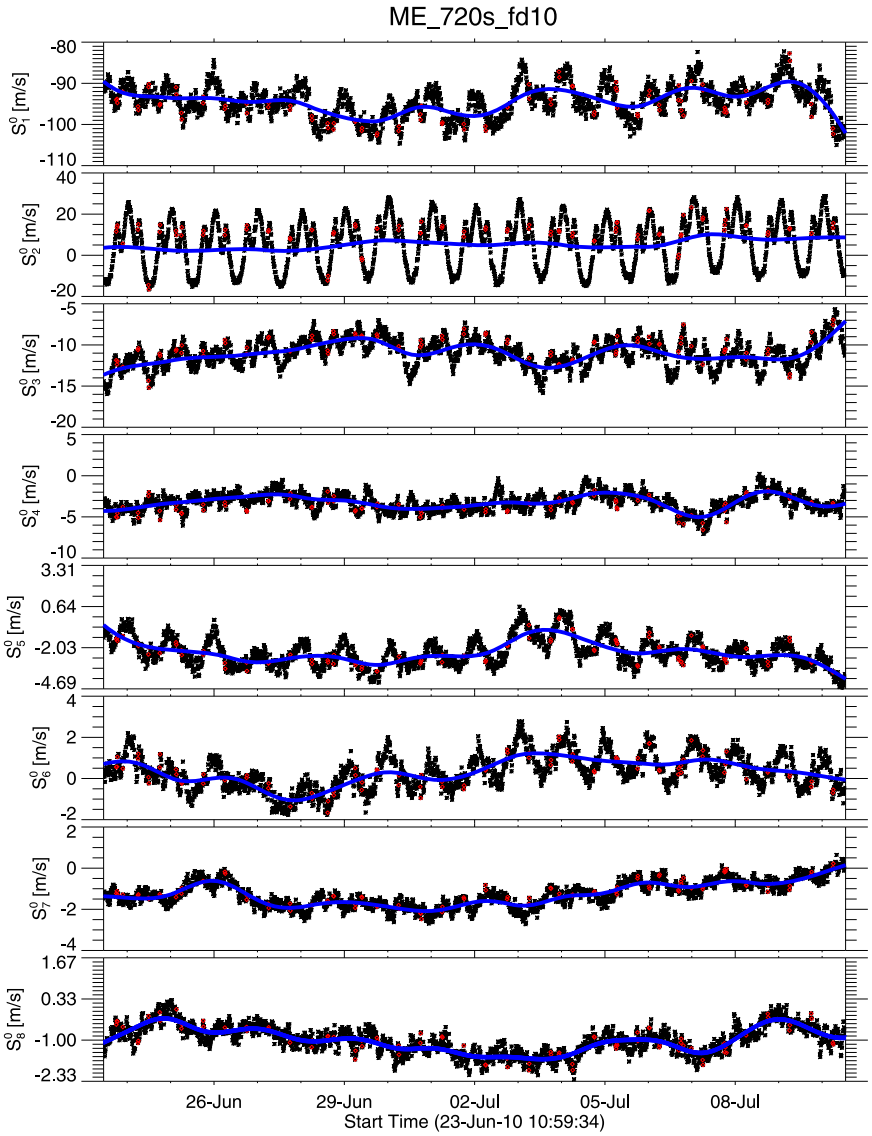

Figure 6. Meridional spectral coefficients during 17 days in 2010. Same format as Figure 4.

where $\oslash$ and $\odot$ represent Hadamard (element-wise) division and multiplication of vectors, respectively. The blue curve in Figure 2 shows the residual spatially averaged rms Doppler velocity for the stage 3 Dopplergrams $\boldsymbol{V}_{\mathrm{LOS}-3}$. Removing the time-varying bias and spatially and temporally adjusting the gain greatly improves the temporal stability of the Dopplergrams. The difference in variability between the black curve (stage 1) and blue curve (stage 3) is roughly 31 dB in power.

Consistent Dopplergrams may then be constructed, adding back the *predicted* bias at a consistent radial velocity $V_{\mathrm{R}} \equiv 0$,

$$\boldsymbol{V}_{\mathrm{LOS}} = \boldsymbol{V}_{\mathrm{LOS}-3} + \mathbf{E}\boldsymbol{\beta}(0, t). \tag{30d}$$

These Dopplergrams are the final result of our COADRED procedure. It is important to note that Equation (30d) does not *correct* the images in an absolute sense; however, it does remove the *inconsistencies* caused by the orbital artifacts.

The reduction in rms velocity shown in Figure 2 is striking. This result indicates that the COADRED procedure is highly effective at removing orbital effects, at least on large scales. The key questions, however, are whether it is robust in that it removes artifacts from all scales and whether it is accurate in that the procedure introduces no new artifacts to the data. In order to answer these questions, we perform below a detailed spectral analysis of the images after each COADRED stage. This analysis shows that the procedure does clean the data from orbital artifacts at all spatial scales and that it does not contaminate the data with new artifacts.

4. ANALYSIS OF STAGES 1–3

SDO produces a significant amount of data, $\simeq$1 TB day^{-1}. Even for the reduced data series considered here, there are 20×10^{10} pixels to analyze over the 17-day period. Further complicating the analysis, data frames are lost in any long data series from *SDO*, and consequently the sample rates are nonuniform. These data require techniques that scale well with $N_{\mathrm{D}} \simeq 10^7$, the number of pixels in each image, and $N_t \simeq 10^3$, the number of images and methods that are either insensitive to the sample rates or explicitly designed to analyze nonuniformly sampled data. For this data set we implement the Karhunen–Loéve (KL) transform (Loéve 1955; Lumley 1967, pp.

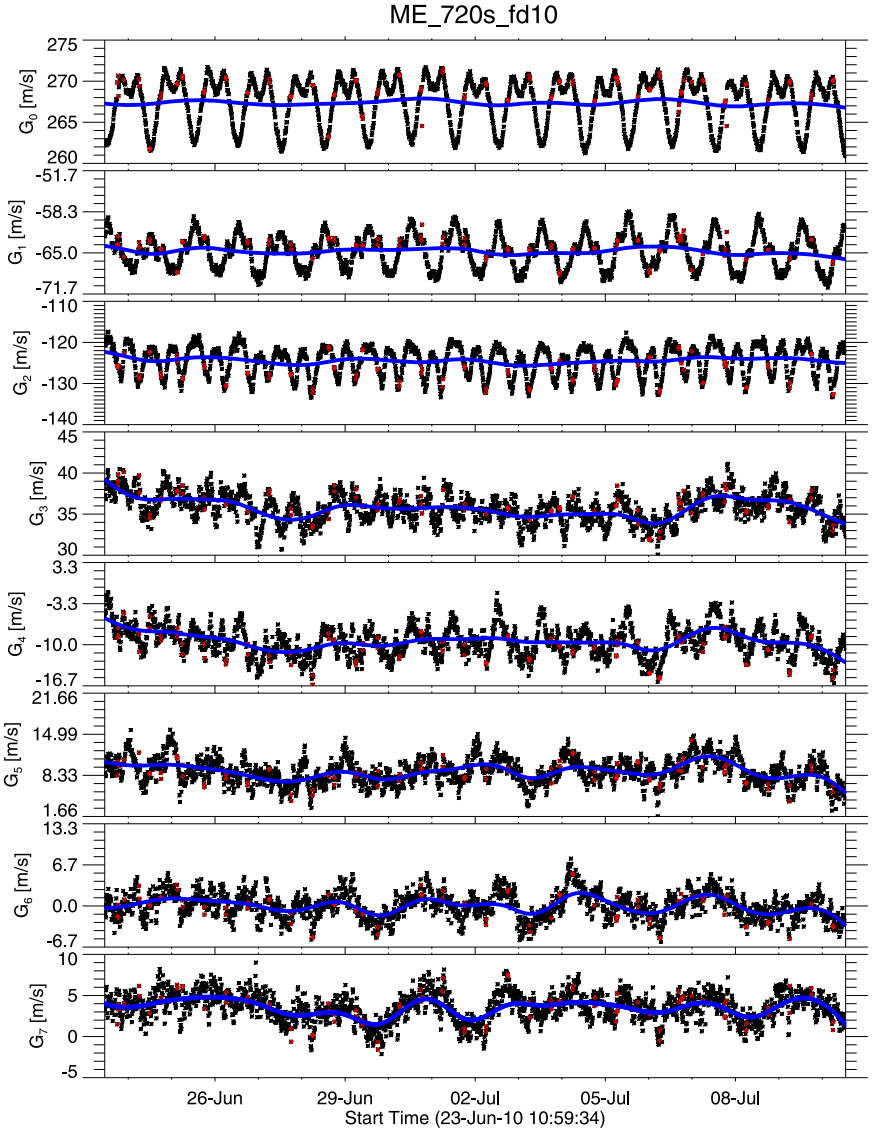

Figure 7. Gain coefficients during 17 days in 2010. Same format as Figure 4.

166–178; Sirovich 1987; Holmes et al. 1996), briefly described in Appendix E, combined with the CLEAN algorithm for computing power spectral density of unevenly sampled time series (Högbom 1974; Roberts et al. 1987). The KL transform decomposes the dynamics into a set of $N_{\rm D} \times N_t$ *orthogonal* spatial modes $\boldsymbol{\Phi}$ and $N_t \times N_t$ *uncorrelated* temporal coefficients $\boldsymbol{\alpha}$ with $N_t \ll N_{\rm D}$.[14] The advantage of the KL transform is that the temporal dynamics of the entire image sequence is represented by a relatively small matrix $\boldsymbol{\alpha}$ in contrast to attempting to interpret spectral properties of $N_{\rm D} \times N_t$ pixels in the image sequence. The disadvantages of the technique are that the spatial information associated with the dynamics is decoupled from the temporal dynamics and the spatial modes are purely empirical—there is not always a simple physical interpretation for the spatial structure of the modes. Using the CLEAN algorithm on the coefficient matrix $\boldsymbol{\alpha}$ completely characterizes the spectral properties of the data as the spatial eigenfunctions $\boldsymbol{\Phi}$ are orthogonal.

[14] $\boldsymbol{\Phi}^\dagger\boldsymbol{\Phi}$ and $\boldsymbol{\alpha}^\dagger\boldsymbol{\alpha}$ are both diagonal matrices, which implies that the dynamics of each individial mode may be considered independently.

The images for each stage are first co-aligned (see Section 2.2), registered, and packed into a data cube or image sequence denoted $\boldsymbol{I}'$, which is $\mathbb{R}^{N_{\rm D}\times N_t}$. The solar disk for images in the sequence is now represented by a packed vector of length $N_{\rm D}$. The temporal median is vector determined for each stage via

$$\langle \boldsymbol{I} \rangle = \text{median}_{N_t}(\boldsymbol{I}'), \tag{31a}$$

where the median image vector $\langle \boldsymbol{I} \rangle$ is understood to be the temporal median of each pixel in N_t images. This median, which contains both time-averaged physical effects and time-averaged artifacts, is then subtracted from each image ($i = 1, N_{\rm D}, j = 1, \ldots, N_t$),

$$(\boldsymbol{I})_{ij} = (\boldsymbol{I}')_{ij} - (\langle \boldsymbol{I} \rangle)_i. \tag{31b}$$

Figure 12 shows the median co-aligned Doppler image (unpacked image vector $\langle \boldsymbol{I} \rangle$) and histogram after various stages of processing: the top is stage 1, the middle is stage 2, and the bottom is stage 3. The stage 1 image is dominated by the time-averaged differential rotation, limb shift, and meridional flow

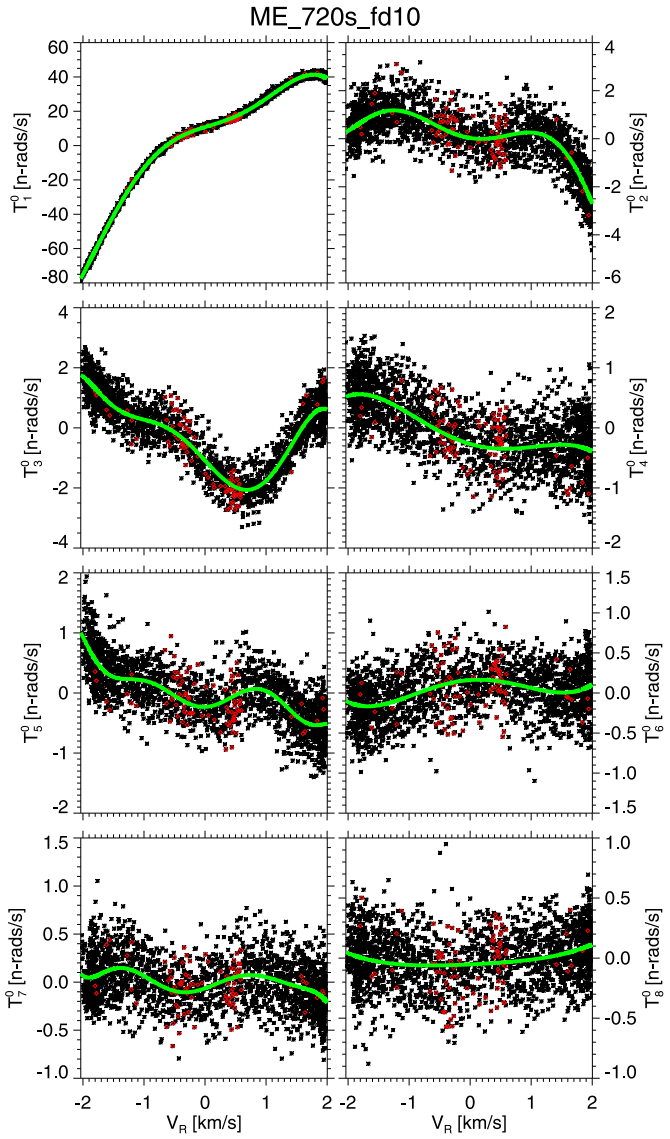

Figure 8. Rotational spectral coefficients during 17 days in 2010 as a function of satellite radial velocity V_R. The black data are "high-quality" data, and the red data are low-quality data (Keyword: QUALITY $\neq 0$). The green line corresponds to the "best" fit of orthogonalized polynomials as determined by the BIC.

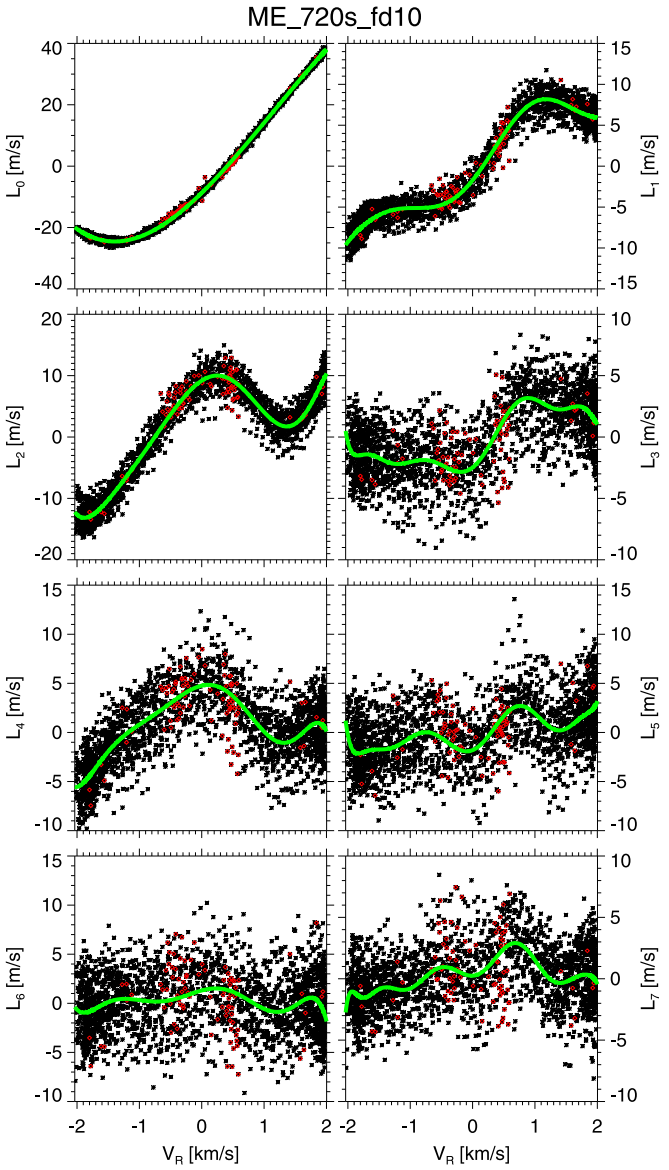

Figure 9. Limb shift spectral coefficients during 17 days in 2010 as a function of satellite radial velocity V_R. Same format as Figure 8.

patterns. The middle and bottom panels exhibit the clear Fresnel artifact reported by Couvidat et al. (2012) superimposed on the horizontal streaks caused by the time-averaged physical behavior of the convective structures. The Fresnel pattern is not an orbital artifact, and it should be reduced or eliminated in HMI data after 2012 October by changes in calibration (personal communication with Todd Hoeksema).

The KL transform is used to decompose the image sequence $\boldsymbol{I}$ into an $\mathbb{R}^{N_t \times N_t}$ matrix of orthogonal coefficients $\boldsymbol{\alpha}$ and an $\mathbb{R}^{N_D \times N_t}$ matrix of orthogonal spatial modes $\boldsymbol{\Phi}$,

$$\boldsymbol{I} = \boldsymbol{\Phi}\, \boldsymbol{\alpha}^{\dagger}. \tag{32}$$

The eigenvalue spectra can be interpreted as "variance explained" or a contribution to the total variance by each of the modes. In general, the KL modes have the following temporal and spatial properties: $\Delta T \simeq 1/\#$ and $\Delta L \simeq 1/\#$, i.e., higher mode numbers (#'s) correspond to faster timescales and smaller spatial scales. The left panel of Figure 13 shows the eigenvalue spectra after the various stages of analysis: 1 (black), 2 (red), and 3 (blue). Stage 1, which contains both orbital artifacts in bias and gain, is consequently significantly different from stages 2 and 3, particularly for the three lowest modes and perhaps as high as mode #5. While the stage 2 (red) and stage 3 (blue) curves appear very similar to each other, this is due to the log–log scale used to display spectra combined with the large fraction of power contained in the time-varying bias—particularly modes #1 and #2 of stage 1 (black). Additionally, because the KL transform empirically determines the spatial eigenmodes from each image set, the spatial eigenmodes change for each stage, and therefore the left panel does not allow for a straightforward comparison of eigenvalues for each mode between stages. To elucidate this, the right panel of Figure 13 shows the eigenvalue spectra of the difference images computed between stage 2 and stage 1 (black), between

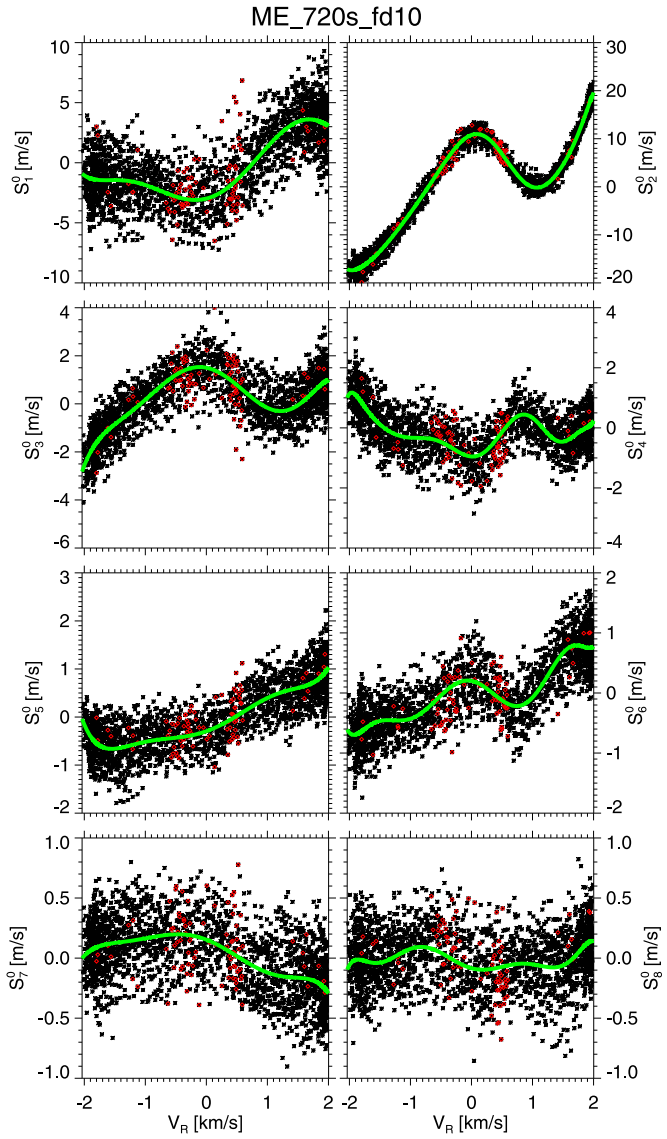

Figure 10. Meridional spectral coefficients during 17 days in 2010 as a function of satellite radial velocity V_R. Same format as Figure 8.

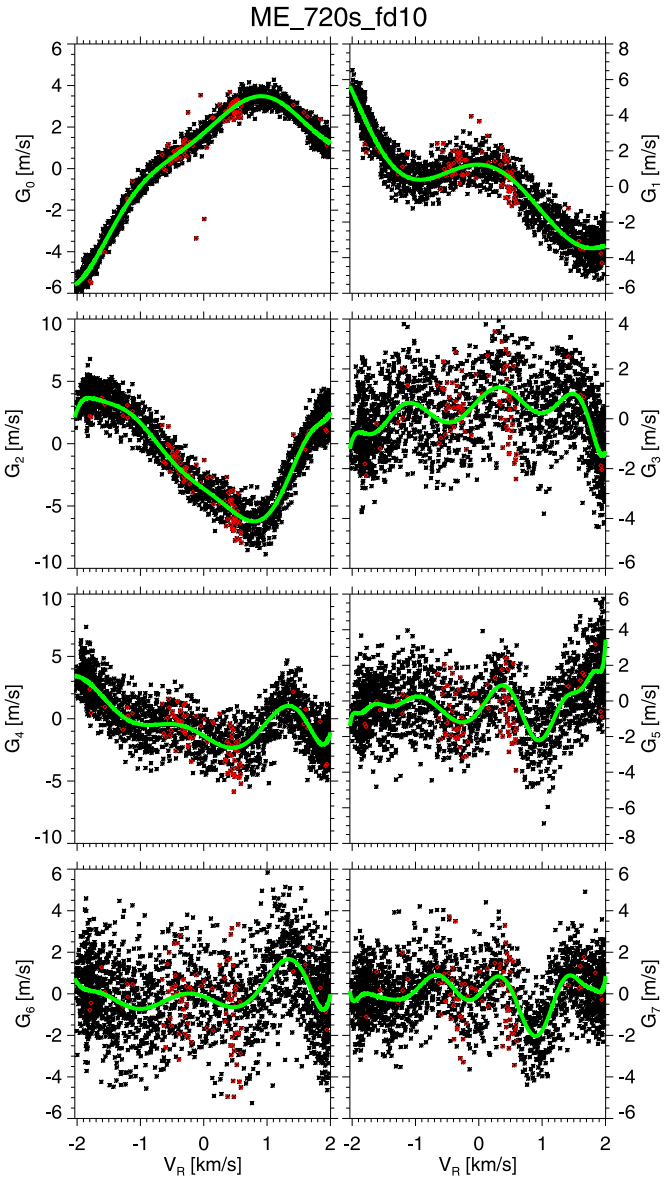

Figure 11. Gain coefficients during 17 days in 2010 as a function of satellite radial velocity V_R. Same format as Figure 8.

stage 3 and stage 2 (red), and between stage 3 and stage 1 (blue). The eigenvalue spectra of the difference images isolate the effect of each adjustment on the Doppler images. The black dashed curve demonstrates that the bias adjustment between stages 2 and 1 is roughly contained in the first 25 (largest-scale) modes. This is consistent with the subtraction of the 32 smooth eigenfunctions used in Section (3.2.4) to represent the bias for each image. In contrast, the gain adjustment between stages 3 and 1, denoted by the red dashed curve, is fairly flat across the modes, with a slow rolloff in the eigenvalues out beyond mode #1000 and a faster rolloff between modes #1500–2045. In this case, the gain adjustment is represented by only eight smooth eigenfunctions; this adjustment corrects the amplitude of all spatial scales in every image as a function of satellite velocity V_R—implying that all spatial and temporal scales, through the dependence on V_R, are contaminated with orbital artifacts. Indeed, 90% of the total variance between stages 3 and 2 is explained by high spatial modes #26–2045. Finally, the blue dashed curve demonstrates the combined effect of the bias subtraction and gain adjustment with a transition between the two effects occurring between modes #10 and #30. Below it is shown that while the gain adjustment only modifies the overall eigenvalue spectra slightly in comparison to the bias subtraction, it dramatically improves the temporal and spectral characteristics of the Doppler image sequence. Figures 14–16 show the spatial eigenfunctions and temporal behavior of the coefficients of modes #1 and #2 for stages 1–3. Note the east-to-west asymmetric distribution of spatial power and the nearly periodic behavior of the coefficients caused by the time-varying bias and gain in Figure 14 for stage 1 in Figure 14. After bias removal in stage 2 and gain adjustment in stage 3, modes #1 and #2 reveal the horizontal streaks associated with the long-time behavior of convective structures—supergranules.

Figure 17 shows the power in the coefficients of the KL transforms (α^2) as a function of time for the stage 1 (left

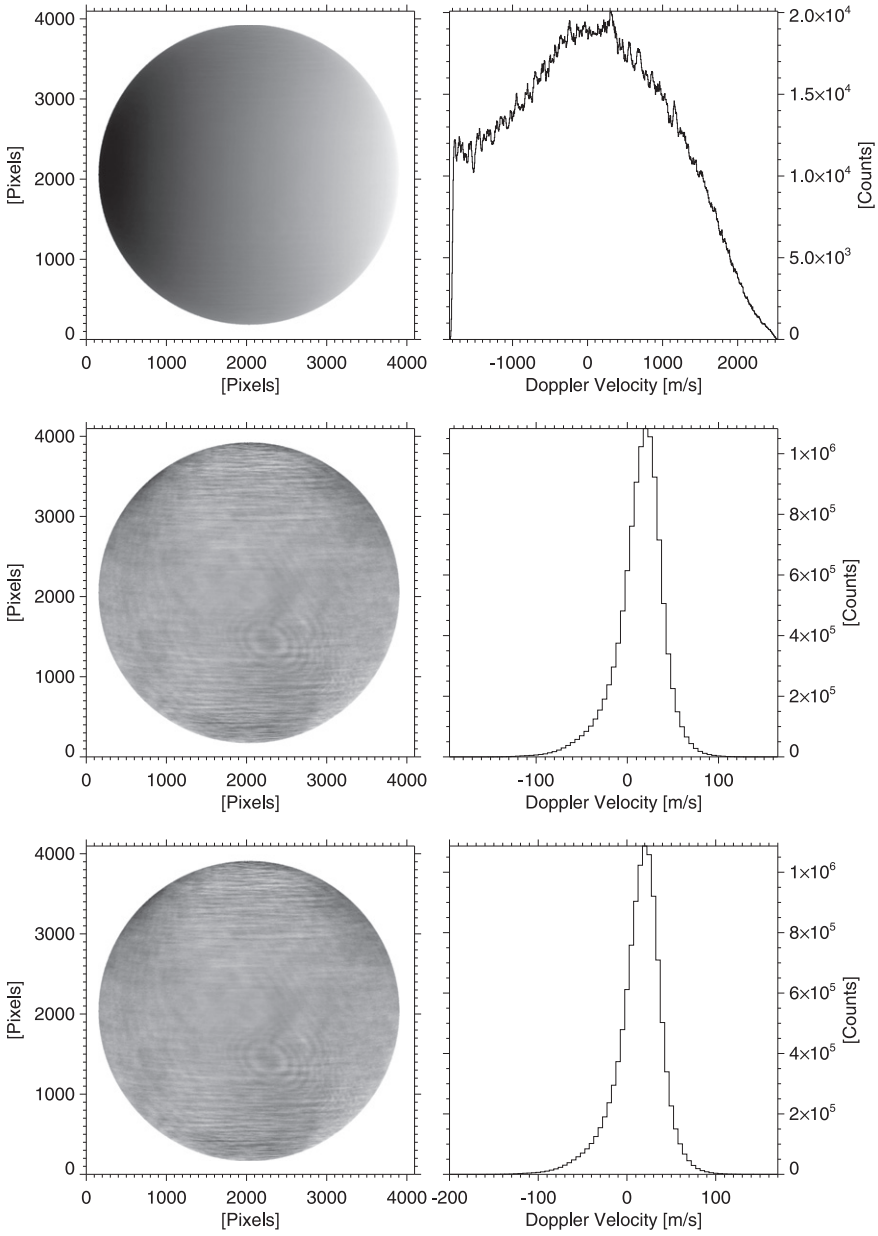

Figure 12. Median co-aligned Doppler image and histogram after various stages of processing: the top is stage 1, the middle is stage 2, and the bottom is stage 3. The stage 1 image is dominated by the time-averaged differential rotation, limb shift, and meridional flow patterns. The middle and bottom panels exhibit a clear Fresnel artifact superimposed on the horizontal steaks caused by the time-averaged behavior of the convective structures.

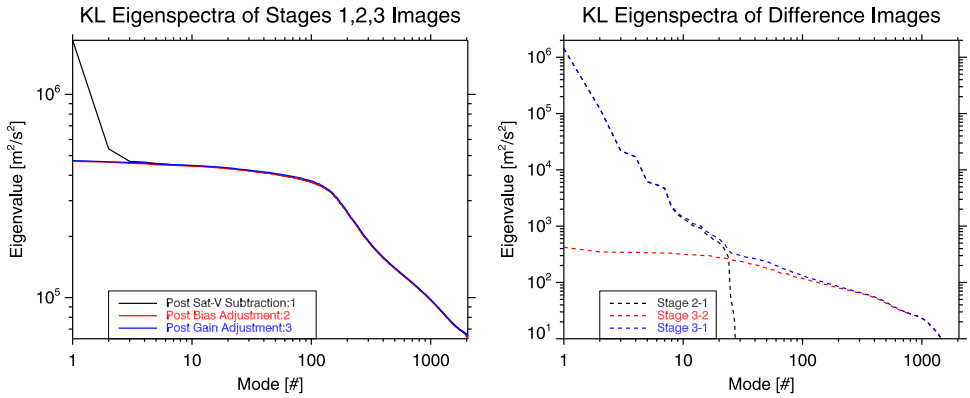

Figure 13. Left: KL eigenvalue spectra after the various stages of analysis: 1 (black), 2 (red), and 3 (blue). Right: KL eigenvalue spectra of the difference images between stages 2 and 1 (black), 3 and 2 (red), and 3 and 1 (blue).

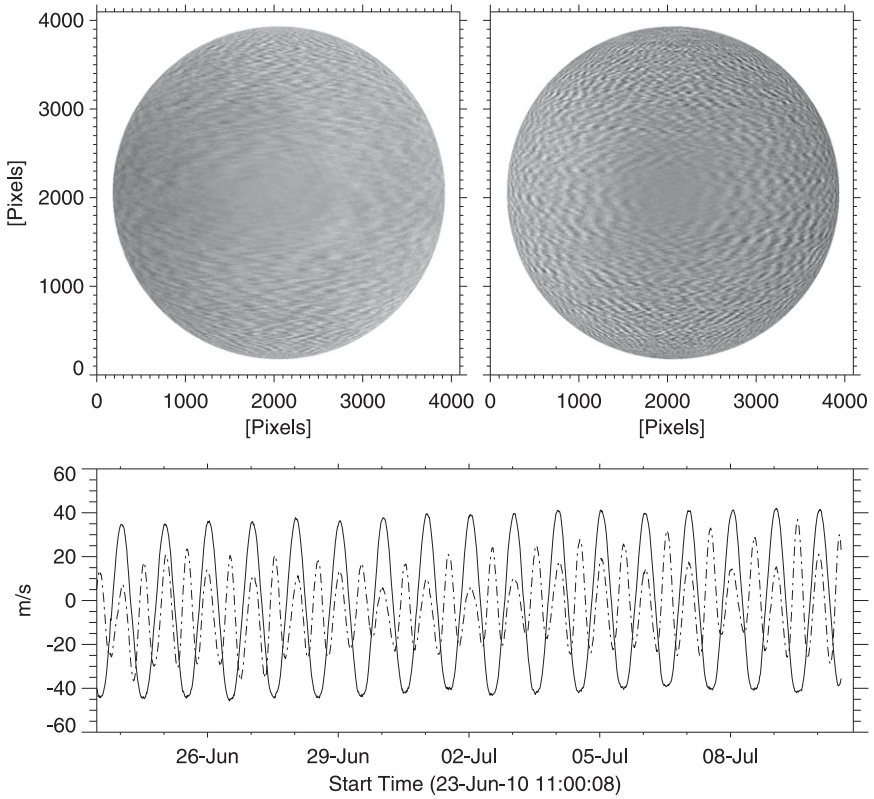

Figure 14. Top: spatial KL modes #1 and #2 for stage 1. Bottom: time history of the coefficients for modes #1 (solid) and #2 (dashed). Note the east-to-west asymmetric distribution of spatial power and the nearly periodic behavior of the coefficients.

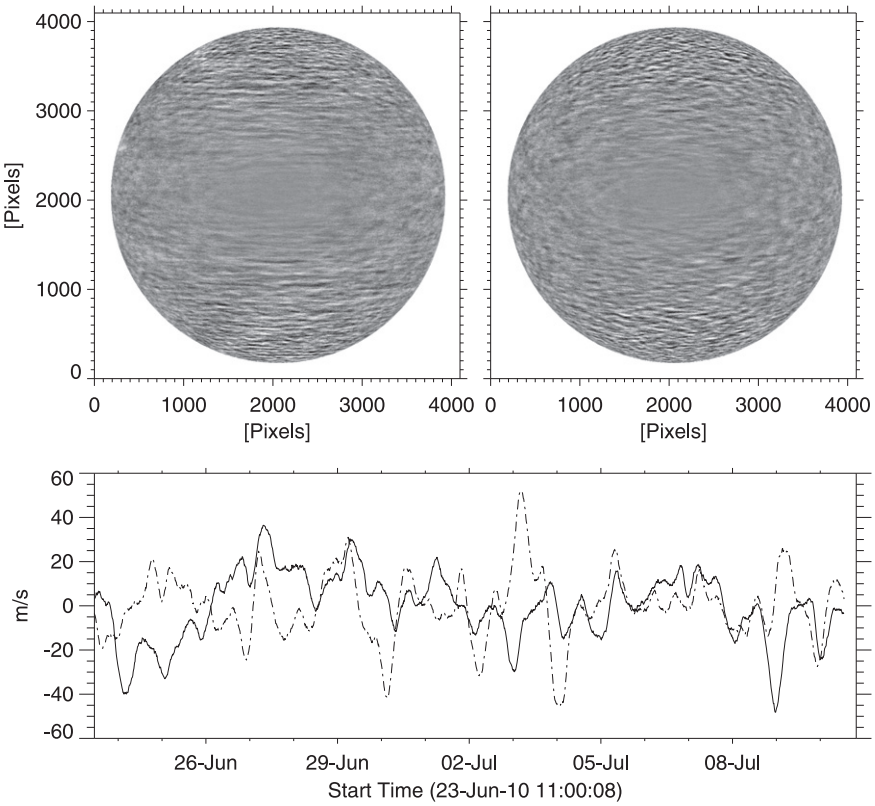

Figure 15. Top: spatial KL modes #1 and #2 for stage 2. Bottom: time history of the coefficients for modes #1 (solid) and #2 (dashed).

column), stage 2 (middle column), and stage 3 (right column) data. The top, middle, and bottom panels correspond to a magnified view of modes #1500–2045, #1–200, and #1–10 for each stage. The behavior of the modes from #100 to 1500 is more easily addressed with the spectra shown in Figure 17. The stage 1 data (left column) exhibit clear daily periodicities

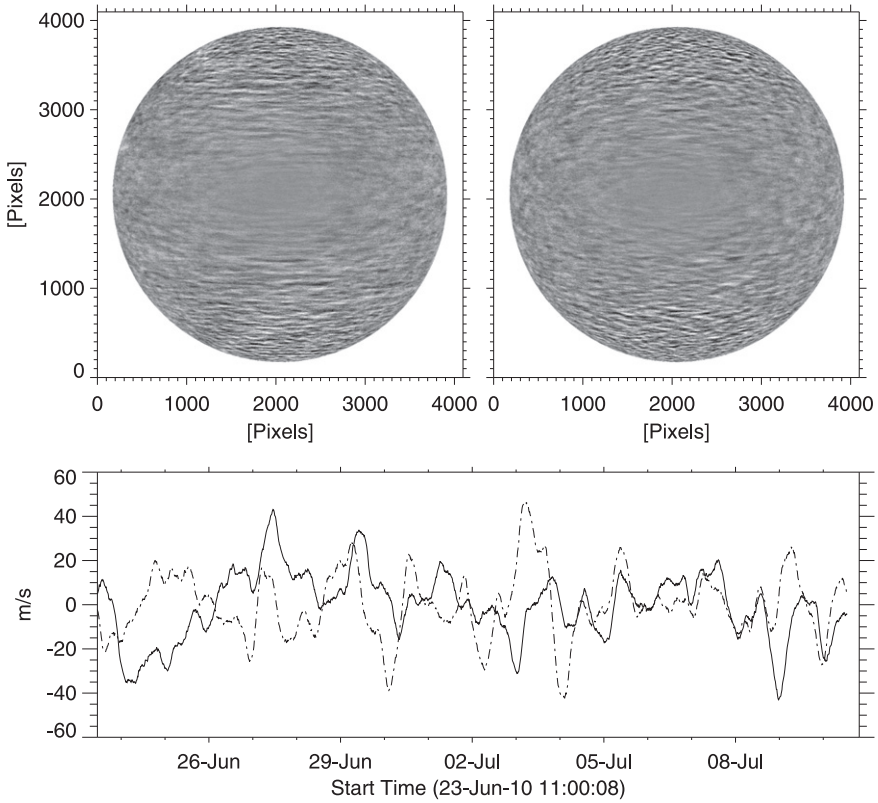

Figure 16. Top: spatial KL modes #1 and #2 for stage 3. Bottom: time history of the coefficients for modes #1 (solid) and #2 (dashed).

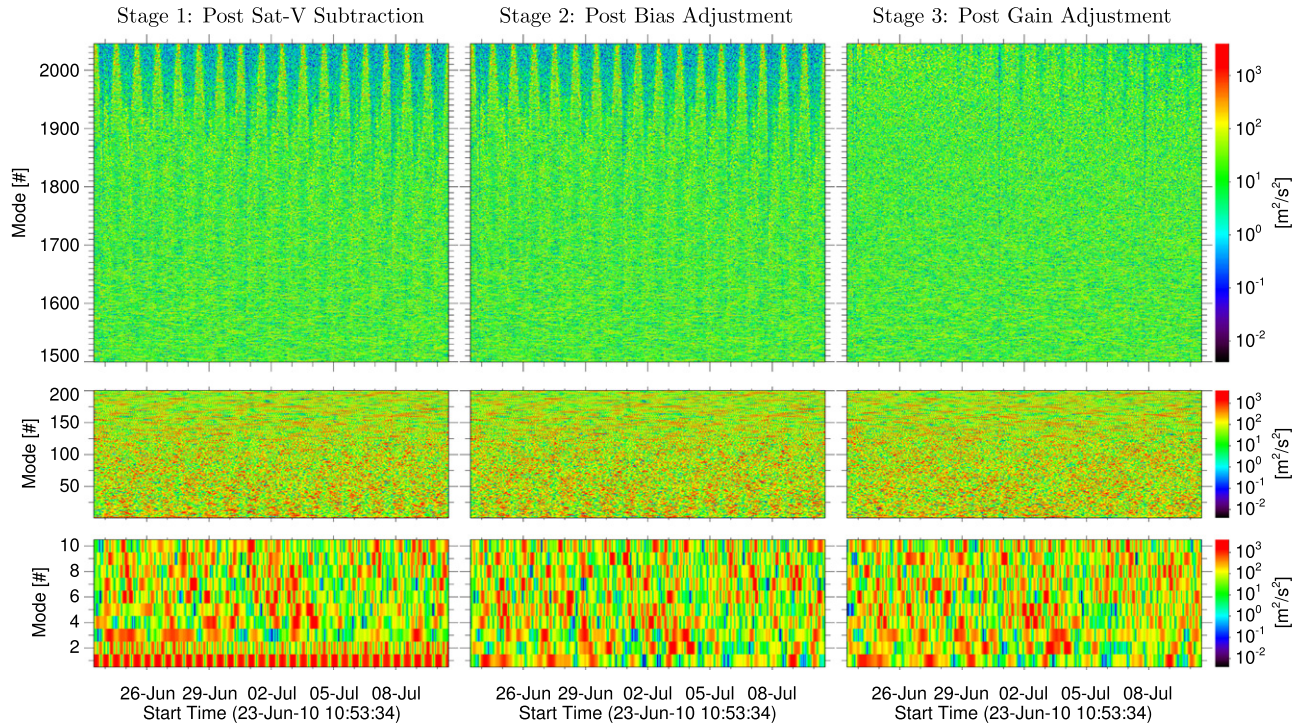

Figure 17. Power in the coefficients of the KL transforms (α^2) for stage 1 (left column), stage 2 (middle column), and stage 3 (right column) data. The top, middle, and bottom panels correspond to a magnified view of modes #1500–2045, #1–200, and #1–10 for each stage.

in modes #1 and #2, as expected from Figure 14, and an overall daily modulation of the power particularly evident below mode #100 and more subtle from modes #100–200 in the middle panel and again quite obvious above mode #1700 in the top panel and more subtle from modes #1500–1700. The stage 2 data (middle column), after the large-scale flows have been removed, is improved at the lowest few modes in the bottom panel, reinforcing the concept that the lowest KL modes

correspond to the slowest timescales and the largest spatial scales. The stage 3 data (right column), after gain adjustment, are dramatically more uniform than the stage 1 and stage 2 data in the top and middle panels. Despite the improvement, there remain some temporal artifacts in the power of the highest mode numbers for the stage 3 data.

The CLEAN algorithm (Högbom 1974; Roberts et al. 1987) is used to estimate the power spectral density of the KL modes for each stage. The CLEAN algorithm performs a nonlinear deconvolution of the unevenly temporally sampled coefficients α in the frequency domain to attempt to minimize the spectral artifacts introduced by the sampling function. Figure 18 shows the power spectral density in the coefficients of the KL transforms (α^2) for stage 1 (left column), stage 2 (middle column), and stage 3 (right column) data estimated using the CLEAN algorithm with a gain of 0.05 and about 1400 iterations. The top row shows the entire spectral range for all of the modes. The middle row is a magnified view of the 10 lowest modes from 0 to 5 cycles day^{-1} for each stage, corresponding to the small box in the lower left corner of the panels in the top row. The bottom row corresponds to a magnified view of the modes #650–1000 from 20 to 30 cycles day^{-1} for each stage, corresponding to the box in the lower middle of each panel in the top row.

The general features of the top panel are a low-frequency 0–5 cycle day^{-1} signature from modes #0–100 with a narrow dispersion relationship $f \simeq \#$ above that. The low-frequency signature is produced by large-scale features moving across the solar disk, whereas the narrow dispersion relation is caused by small-scale convective features moving across the disk. This narrow dispersion relationship exhibits harmonics above mode #200. The spectral signatures of the orbital artifacts in the large-scale flows is exhibited in the middle panel of the first column. Significant isolated spectral peaks are present at 1 and 2 cycles day^{-1} in mode #1 and at 1, 2, and 3 cycles day^{-1} in mode #2. There are also harmonics at 1, 2, and 3 cycles day^{-1} near mode #400 in the top left panel. These spectral signatures are largely mitigated after the removal of the large-scale flow bias, as shown by the panels in the middle and right columns. However, what remains (shown particularly well in the middle column) are multiple harmonics of the relatively narrow dispersion relationship $f \simeq \#$. These harmonics are caused by the modulation in the amplitude of convective structures as they rotate across the disk. The stage 3 data show that the spatially and temporally dependent gain adjustment included in Equation (26) considerably reduces the effect of this modulation by collapsing the harmonics to a single peak at $f \simeq \#$.

5. DISCUSSION AND CONCLUSIONS

We have presented and characterized a method to reduce and mitigate the orbital artifacts from the Dopplergrams as retrieved from the HMI Milne–Eddington inversion output. It is important to note that the stage 3 data cannot be claimed to be *more accurate*, only that they are *more consistent* from Dopplergram to Dopplergram. There are still artifacts that remain in the data shown in the right column of Figures 17 and 18; however, this is clearly a dramatic improvement in the quality of the Doppler data. While it is well known that the Milne–Eddington inversion of the HMI pipeline data contains orbital artifacts up to harmonics of several cycles day^{-1} (Hoeksema et al. 2014), the important takeaway from the left column of Figures 17 and 18 is that *all temporal and spatial scales are contaminated by the orbital artifacts!* We know of no simple postprocessing that will filter each spatial scale appropriately to remove the harmonics. It would be very surprising if the same conclusion did not also apply to the other critical observables produced by the Milne–Eddington inversion of the HMI pipeline data such as the magnetic field data. Furthermore, if similar contamination is present in the 45 s Dopplergrams observed by Camera #2, we speculate that the modulation of the observations will affect the amplitude of the 5-minute oscillations critical to helioseismic observations.

The important new result of this paper is that the COADRED procedure does successfully remove the orbital artifacts in the HMI Doppler data. Figure 2 shows that the improvement in the data is dramatic; the daily oscillations are almost completely eliminated. Furthermore, the procedure is robust in that, as shown by Figure 18, it cleans the data on all spatial scales *without introducing new artifacts*. The COADRED procedure is straightforward to implement and will work on any data set of HMI Dopplergrams; consequently, we recommend that our procedure, or some modification, be incorporated into any HMI data analysis investigation. A key feature of the procedure is the use of the limb shift eigenfunctions to correct the gain in each pixel. The fact that this gain correction is so successful has major implications for the possible mechanisms giving rise to the HMI errors and, consequently, for removing these errors from the vector magnetograms as well. If we can correct the vector magnetograms to the same level of fidelity as that shown by Figures 2 and 18, the resulting data would be invaluable for studying solar structure and dynamics.

P.W.S. acknowledges the support of the NASA LWS and GI programs and NASA/GSFC bridge funding in completing this work. He also gratefully acknowledges useful conversations with Peter Williams, Mark Linton, Jesper Schou, David Hathaway, Yang Liu, Todd Hoeksema, and Phil Scherrer. K.D.L., G.B., and P.W.S. were supported by NASA GI contracts NNH12CG10C ("Photospheric Properties of Flaring versus Flare-Quiet Active Regions: Can We Use HMI Vector Magnetogram Sequences to Quantify When and Why Does the Sun Go Boom?") and NNH12CC03C ("Using SDO/HMI Data to Investigate the Energization of the Coronal Magnetic Field"). We also gratefully acknowledge the help of Steve Martin, who configured "houdini," our 80-core, 2 TB shared memory system, which was indispensable in the calculations. We also acknowledge the use of GNU Parallel (Tange 2011).

APPENDIX A
OBSERVER MOTION

Using heliocentric Cartesian coordinates (x, y, z), the z-axis is defined along the axis parallel to the observer–Sun line, pointing toward the observer. The y-axis is define to be perpendicular to that line and in the plane with the z-axis and the solar north pole, with y increasing toward solar north. The x-axis is defined to be perpendicular to both the y- and z-axes, with x increasing toward solar west. The location of a feature on the disk is given by (see Equation (17) in Thompson 2006)

$$x = -d \sin\theta_\rho \sin\psi, \tag{33a}$$

$$y = d \sin\theta_\rho \cos\psi, \tag{33b}$$

$$z = D_\odot - d \cos\theta_\rho, \tag{33c}$$

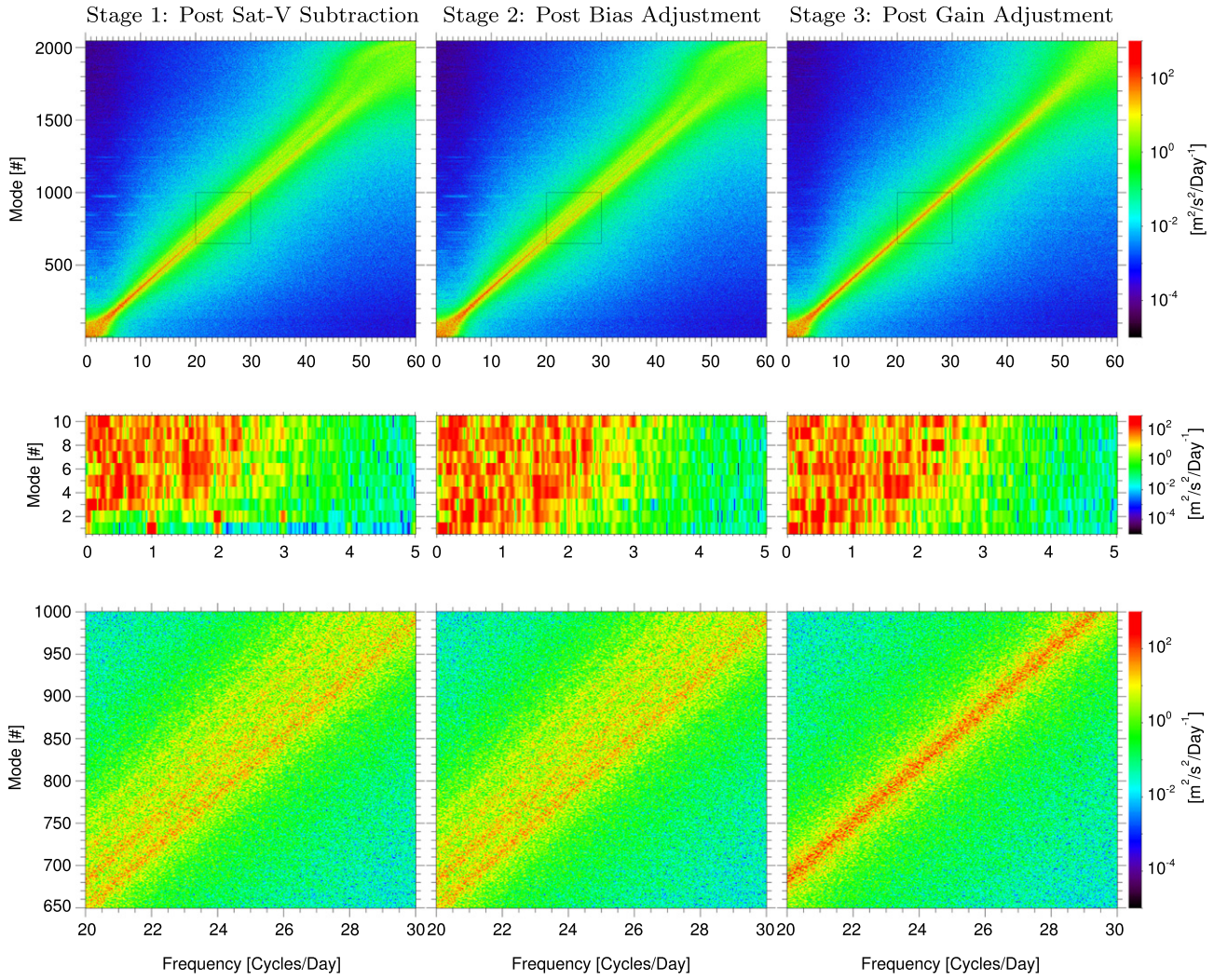

Figure 18. Power spectral density in the coefficients of the KL transforms (α^2) for stage 1 (left column), stage 2 (middle column), and stage 3 (right column) data estimated using the CLEAN algorithm with a gain of 0.05 and about 1400 iterations. The middle row corresponds to a magnified view of the 10 lowest modes from 0 to 5 cycles day^{-1} for each stage, corresponding to the small box in the lower left corner of the panels in the top row. The bottom row is a magnified view of the modes #650–1000 from 20 to 30 cycles day^{-1}for each stage, corresponding to the box in the lower middle of each panel in the top row.

where θ_ρ is the helioprojective angle, ψ is the position angle defined counterclockwise from solar north, d is the distance between the feature and the observer, and $D_\odot$ is the distance between the observer and Sun center. The LOS vector pointing *from* the feature *to* the observer is then (as shown in Equation (1) repeated here for reference)

$$\hat{\boldsymbol{\eta}}_{\rm LOS}(\theta_\rho, \psi) = \sin\theta_\rho \sin\psi\, \hat{\boldsymbol{x}} - \sin\theta_\rho \cos\psi\, \hat{\boldsymbol{y}} + \cos\theta_\rho\, \hat{\boldsymbol{z}}.$$

This implies that the raw observed Doppler velocity for stage 0 at each pixel i can be expressed as

$$v_{{\rm LOS}-0,i} = \hat{\boldsymbol{\eta}}_{\rm LOS} \cdot \boldsymbol{V}_{SDO} - \hat{\boldsymbol{\eta}}_{\rm LOS} \cdot \boldsymbol{U}_{\rm surface}, \tag{34}$$

and the stage 1 data with the satellite velocity subtracted, or the "V-sat subtracted" data, may be expressed as (as shown in Equation (2) repeated here for reference)

$$v_{{\rm LOS}-1,i} = v_{{\rm LOS}-0,i} - \hat{\boldsymbol{\eta}}_{\rm LOS} \cdot \boldsymbol{V}_{SDO} \equiv -\hat{\boldsymbol{\eta}}_{\rm LOS} \cdot \boldsymbol{U}_{\rm surface}.$$

APPENDIX B
STONYHURST UNIT VECTORS

Since we are describing the Sun in Stonyhurst coordinates, the unit vectors must be determined to resolve the projection of various vector quantities onto the LOS. The transformation between Stonyhurst and heliocentric Cartesian coordinates is

$$x = r\,[\cos\Theta \sin(\Phi - \Phi_0)], \tag{35a}$$

$$y = r\,[\sin\Theta \cos B_0 - \cos\Theta \cos(\Phi - \Phi_0) \sin B_0], \tag{35b}$$

$$z = r\,\sin\Theta \sin B_0 + \cos\Theta \cos(\Phi - \Phi_0) \cos B_0, \tag{35c}$$

where Θ and Φ are the latitude and longitude, respectively, B_0 is the so-called solar-B angle (the latitude of the center of the solar disk as seen by the observer), and Φ_0 is the Carrington longitude of the center of the solar disk. The gradient in Stonyhurst coordinates is given by

$$\boldsymbol{\nabla} = \widehat{\boldsymbol{\Phi}} \frac{1}{r\cos\Theta} \partial_\Theta + \widehat{\boldsymbol{\Theta}} \frac{1}{r} \partial_r + \hat{\boldsymbol{r}}\, \partial_r. \tag{36}$$

The Jacobian of transformation between heliocentric Cartesian unit vectors and Stonyhurst unit vectors is then

$$\mathcal{J} = \boldsymbol{\nabla}(x, y, z), \tag{37a}$$

$$= \begin{pmatrix} \cos\Phi & \sin B_0 \sin\Phi & -\cos B_0 \sin\Phi \\ -\sin\Phi \sin\Theta & \cos B_0 \cos\Theta + \cos\Phi \sin B_0 \sin\Theta & \cos\Theta \sin B_0 - \cos B_0 \cos\Phi \sin\Theta \\ \cos\Theta \sin\Phi & \cos B_0 \sin\Theta - \cos\Phi \cos\Theta \sin B_0 & \cos B_0 \cos\Phi \cos\Theta + \sin B_0 \sin\Theta \end{pmatrix} \tag{37b}$$

where $\mathcal{J}$ transforms heliocentric Cartesian to Stonyhurst unit vectors and $\mathcal{J}^{\mathrm{T}}$ vice versa:

$$(\widehat{\boldsymbol{\Phi}}, \widehat{\boldsymbol{\Theta}}, \hat{\boldsymbol{r}})^{\mathrm{T}} = \mathcal{J} \cdot (\hat{\boldsymbol{x}}, \hat{\boldsymbol{y}}, \hat{\boldsymbol{z}})^{\mathrm{T}}, \tag{38a}$$

$$(\hat{\boldsymbol{x}}, \hat{\boldsymbol{y}}, \hat{\boldsymbol{z}})^{\mathrm{T}} = \mathcal{J}^{\mathrm{T}} \cdot (\widehat{\boldsymbol{\Phi}}, \widehat{\boldsymbol{\Theta}}, \hat{\boldsymbol{r}})^{\mathrm{T}}. \tag{38b}$$

These unit vectors can be combined with Equation (1) to determine the projection of the Stonyhurst unit vectors onto the LOS:

$$\hat{\boldsymbol{\eta}}_{\mathrm{LOS}} \cdot \mathcal{J}^{\mathrm{T}} \cdot \widehat{\boldsymbol{\Phi}} = -\cos B_0 \sin\Phi \cos\theta_\rho + (\cos\Phi \sin\psi - \sin B_0 \sin\Phi \cos\psi) \sin\theta_\rho, \tag{39a}$$

$$\hat{\boldsymbol{\eta}}_{\mathrm{LOS}} \cdot \mathcal{J}^{\mathrm{T}} \cdot \widehat{\boldsymbol{\Theta}} = (\sin B_0 \cos\Theta - \cos B_0 \cos\Phi \sin\Theta) \cos\theta_\rho - [\sin\Phi \sin\Theta \sin\psi + (\sin B_0 \cos\Phi \sin\Theta + \cos B_0 \cos\Theta) \cos\psi] \sin\theta_\rho \tag{39b}$$

$$\hat{\boldsymbol{\eta}}_{\mathrm{LOS}} \cdot \mathcal{J}^{\mathrm{T}} \cdot \hat{\boldsymbol{r}} = (\cos B_0 \cos\Phi \cos\Theta + \sin B_0 \sin\Theta) \cos\theta_\rho + [\sin\Phi \cos\Theta \sin\psi - (\cos B_0 \sin\Theta - \sin B_0 \cos\Phi \cos\Theta) \cos\psi] \sin\theta_\rho. \tag{39c}$$

APPENDIX C
HELIOCENTRIC COORDINATES FOR MERIDIONAL FLOWS AND THE CONVECTIVE BLUESHIFT

The convective blueshift is conventionally described in heliocentric spherical coordinates, where ϱ is the angle between the point on the solar surface and the line connecting Sun center to the observer ($\hat{\boldsymbol{z}}$-axis):

$$x = -R_\odot \sin\varrho \sin\psi, \tag{40a}$$

$$y = R_\odot \sin\varrho \cos\psi, \tag{40b}$$

$$z = R_\odot \cos\varrho. \tag{40c}$$

Equating Equations (33*a*) and (40*a*), we can obtain the law sines for the relationship between the angles

$$\frac{\sin\varrho}{d} = \frac{\sin\theta_\rho}{R_\odot} = \frac{\sin[\pi - (\varrho + \theta_\rho)]}{D_\odot}, \tag{41}$$

where the last relationship is determined from the law of sines. Rearranging, we have (see pp. 174–175 in Smart 1977)

$$\sin(\varrho + \theta_\rho) = \frac{D_\odot}{R_\odot} \sin\theta_\rho \tag{42a}$$

or

$$\varrho = \sin^{-1}\left(\frac{D_\odot}{R_\odot} \sin\theta_\rho\right) - \theta_\rho. \tag{42b}$$

From Equations (35*a*–35*c*) and (40*a*–40*c*) we obtain the relations between Stonyhurst and heliocentric spherical coordinates

$$\sin\Theta = \sin B_0 \cos\varrho + \cos B_0 \sin\varrho \cos\psi, \tag{43a}$$

$$\cos\Theta \sin\Phi = -\sin\varrho \sin\psi, \tag{43b}$$

$$\cos\Theta \cos\Phi = \cos B_0 \cos\varrho - \sin B_0 \sin\varrho \cos\psi. \tag{43c}$$

APPENDIX D
EVALUATION OF HATHAWAY'S INTEGRAL

$$G_{\mathrm{MF},\ell}(B_0, \varrho) = \frac{1}{2\pi} \int_0^{2\pi} d\psi\, \hat{\boldsymbol{\eta}}_{\mathrm{LOS}} \cdot \mathcal{J}^{\mathrm{T}} \cdot \widehat{\boldsymbol{\Theta}}\, \overline{P}_\ell^1(\sin\Theta).$$

Equation (18) (repeated above for reference) is a complicated integral to evaluate given that Θ and Φ must be reexpressed as functions of ϱ and ψ. Noting that the associated Legendre function may be expressed in terms of the Legendre function of order zero ($m = 0$),

$$P_\ell^m(x) = (-1)^m (1 - x^2)^{m/2} \frac{d^m}{dx^m} P_\ell(x), \tag{44}$$

and using a lemma for the expansion of the derivative of Legendre functions $P_\ell^m(x)$ (see Garfinkel 1964),

$$\frac{dP_\ell(x)}{dx} = \sum_{n=0}^{(\ell-1)/2} (2\ell - 4n - 1) P_{\ell-1-2n}(x), \tag{45}$$

the associated Legendre function of order 1 may be expressed as a terminating series of Legendre functions of order 0:

$$P_\ell^1(x) = -\sqrt{1 - x^2} \sum_{n=0}^{(\ell-1)/2} (2\ell - 4n - 1) P_{\ell-1-2n}(x). \tag{46}$$

Substituting $x = \sin\Theta$,

$$P_\ell^1(\sin\Theta) = -\cos\Theta \sum_{n=0}^{(\ell-1)/2} (2\ell - 4n - 1) P_{\ell-1-2n}(\sin\Theta), \tag{47}$$

and using the spherical harmonic addition theorem,

$$P_\ell(\sin\Theta) = \frac{4\pi}{2\ell + 1} \sum_{m=-\ell}^{\ell} Y_\ell^m(B_0, \psi/2) Y_\ell^{m*}(\varrho, -\psi/2),$$
$$= \frac{2}{2\ell + 1} \sum_{m=-\ell}^{\ell} \overline{P}_\ell^m(\sin B_0) \overline{P}_\ell^m(\cos\varrho) e^{im\psi}, \tag{48}$$

this becomes

$$P_\ell^1(\sin\Theta) = -2\cos\Theta \sum_{n=0}^{(\ell-1)/2} \sum_{m=-(\ell-1-2n)}^{\ell-1-2n} \times \overline{P}^m_{\ell-1-2n}(\sin B_0)\overline{P}^m_{\ell-1-2n}(\cos\varrho)e^{i\,m\,\psi} \quad (49)$$

where ψ is now external to the Legendre functions. Using Equation (8),

$$\overline{P}_\ell^1(x) = -\sqrt{\frac{(2\ell+1)(\ell-1)!}{2(\ell+1)!}}\,P_\ell^1(x), \quad (50)$$

we obtain a form consistent with Equation (18),

$$\overline{P}_\ell^1(\sin\Theta) = 2\cos\Theta\sqrt{\frac{(2\ell+1)(\ell-1)!}{2(\ell+1)!}} \sum_{n=0}^{(\ell-1)/2} \sum_{m=-(\ell-1-2n)}^{\ell-1-2n} \times \overline{P}^m_{\ell-1-2n}(\sin B_0)\overline{P}^m_{\ell-1-2n}(\cos\varrho)e^{i\,m\,\psi}. \quad (51)$$

Thus, the integral may be evaluated as

$$G_{\mathrm{MF},\ell}(B_0,\,\varrho) = 2\sqrt{\frac{(2\ell+1)(\ell-1)!}{2(\ell+1)!}} \sum_{n=0}^{(\ell-1)/2} \sum_{m=-(\ell-1-2n)}^{\ell-1-2n} \times \overline{P}^m_{\ell-1-2n}(\sin B_0)\overline{P}^m_{\ell-1-2n}(\cos\varrho) \times [I_1^m(B_0,\,\rho)\cos\theta_\rho - I_2^m(B_0,\,\rho)\sin\theta_\rho], \quad (52)$$

where

$$I_1^m(B_0,\,\rho) = \frac{1}{2\,\pi}\int_0^{2\,\pi} d\psi\; e^{i\,m\,\psi}\cos\Theta \times (\sin B_0\cos\Theta - \cos B_0\sin\Theta\cos\Phi),$$

$$I_2^m(B_0,\,\rho) = \frac{1}{2\,\pi}\int_0^{2\,\pi} d\psi\; e^{i\,m\,\psi}\cos\Theta[\sin\Theta\sin\Phi\sin\psi + (\sin B_0\sin\Theta\cos\Phi + \cos B_0\cos\Theta)\cos\psi]. \quad (53a)$$

Evaluating the first integral,

$$I_1^m(B_0,\,\varrho) = \frac{1}{2\,\pi}\int_0^{2\,\pi} d\psi\; e^{i\,m\,\psi}\cos\Theta(\sin B_0\cos\Theta - \cos B_0\sin\Theta\cos\Phi),$$
$$= \frac{\sin\varrho}{2\,\pi}\int_0^{2\,\pi} d\psi\; e^{i\,m\,\psi}(\sin B_0\sin\varrho - \cos B_0\cos\varrho\cos\psi),$$
$$= (-1)^{m+1}\sin\varrho\,[(2m^2-1)\cos(B_0+\varrho) + \cos(B_0-\varrho)]\,\frac{\sin(m\,\pi)}{2\pi m(m^2-1)},$$
$$= \delta_{m,0}\sin B_0\sin^2\varrho - \frac{1}{2}\,\delta_{|m|,1}\cos B_0\sin\varrho\cos\varrho. \quad (54a)$$

Similarly,

$$I_2^m(B_0,\,\varrho) = \delta_{m,0}\sin B_0\sin\varrho\cos\varrho - \frac{1}{2}\,\delta_{|m|,1}\cos B_0\cos^2\varrho. \quad (54b)$$

Noting that $I_2^m(B_0,\,\varrho) = -\cot\varrho\; I_1^m(B_0,\,\varrho)$,

$$G_{\mathrm{MF},\ell}(B_0,\,\varrho) = (\cos\theta_\rho + \cot\varrho\,\sin\theta_\rho) \times 2\sqrt{\frac{(2\ell+1)(\ell-1)!}{2(\ell+1)!}} \sum_{m=-1}^{1} I_1^m(B_0,\,\varrho) \times \sum_{n=0}^{(\ell-1)/2} \overline{P}^m_{\ell-1-2n}(\sin B_0)\overline{P}^m_{\ell-1-2n}(\cos\varrho). \quad (55)$$

Noting the symmetry property of the Legendre functions

$$P_\ell^{-m}(x) = (-1)^m\,\frac{(\ell-m)!}{(\ell+m)!}\,P_\ell^m(x), \quad (56a)$$

$$\overline{P}_\ell^{-m}(x) = (-1)^m\,\overline{P}_\ell^m(x), \quad (56b)$$

$$G_{\mathrm{MF},\ell}(B_0,\,\varrho) = \sqrt{\frac{2}{2\ell+1}}\,\sin(\varrho+\theta_\rho)\sqrt{1+2\ell}\,\sqrt{\frac{2\ell+1}{\ell(\ell+1)}} \times \sum_{n=0}^{(\ell-1)/2}[\overline{P}^0_{\ell-1-2n}(\sin B_0)\overline{P}^0_{\ell-1-2n}(\cos\varrho)\sin B_0\sin\varrho - \overline{P}^1_{\ell-1-2n}(\sin B_0)\overline{P}^1_{\ell-1-2n}(\cos\varrho)\cos B_0\cos\varrho]. \quad (57)$$

Employing an inductive proof, this generally becomes

$$G_{\mathrm{MF},0}(B_0,\,\varrho) = 0, \quad (58)$$

$$G_{\mathrm{MF},1}(B_0,\,\varrho) = \sqrt{\frac{2}{3}}\,\sin(\varrho+\theta_\rho)\frac{3}{2\sqrt{2}}\,\sin B_0\sin\varrho, = \sqrt{\frac{2}{3}}\,\sin(\varrho+\theta_\rho)\overline{P}_1^0(\sin B_0)\overline{P}_1^1(\cos\varrho), \quad (59)$$

$$G_{\mathrm{MF},2}(B_0,\,\varrho) = \sqrt{\frac{2}{5}}\,\sin(\varrho+\theta_\rho)\frac{5}{8}\,\sqrt{\frac{3}{2}}\,[1-3\cos(2\,B_0)]\sin\varrho\cos\varrho, = \sqrt{\frac{2}{5}}\,\sin(\varrho+\theta_\rho)\overline{P}_2^0(\sin B_0)\overline{P}_2^1(\cos\varrho), \quad (60)$$

and generally

$$G_{\mathrm{MF},\ell}(B_0,\,\varrho) = \sqrt{\frac{2}{2\ell+1}}\,\sin(\varrho+\theta_\rho)\overline{P}_\ell(\sin B_0)\overline{P}_\ell^1(\cos\varrho), \quad (61)$$

where $\theta_\rho \approx 0$ corresponds to the results of Hathaway (1992).

APPENDIX E
KARHUNEN-LO'EVE (KL) ANALYSIS

The KL analysis (Loéve 1955) is known by various names: principle component analysis, proper orthogonal decomposition, empirical orthogonal functions, and/or the Hoteling transform. The approach presented here follows the method of snapshots (Lumley 1967; Sirovich 1987; Holmes et al. 1996). The goal of KL is to determine an optimal representation for the data—optimal in the sense that the vector $\mathbf{d}$ maximizes the projection onto the median-subtracted $\mathbb{R}^{N_\mathrm{D}\times N_t}$ image array $\boldsymbol{I}$. This optimality can be expressed by the functional

$$\mathcal{J}(\mathbf{d}) = N_\mathrm{D}^{-1}\,\mathbf{d}^\dagger\,\boldsymbol{I}^\dagger\,\boldsymbol{I}\,\mathbf{d} - \lambda(\mathbf{d}^\dagger\cdot\mathbf{d} - 1), \tag{62}$$

where † represents the conjugate transpose for complex data or just the transpose for real data, as is being considered here, and the constraint ensures normalization. The $\mathbb{C}^{N_t\times N_t}$ spatially averaged covariance matrix of the image sequence is defined as

$$\mathcal{C} \equiv \frac{\boldsymbol{I}^\dagger\,\boldsymbol{I}}{N_\mathrm{D}}, \tag{63a}$$

$$\mathcal{C}_{nm} = \frac{1}{N_\mathrm{D}}\sum_{i=1}^{N_\mathrm{D}}[\boldsymbol{I}^\dagger]_{ni}\,[\boldsymbol{I}]_{im}, \tag{63b}$$

which permits the expression of the functional

$$\begin{aligned}\mathcal{J}(\mathbf{d}+\delta\boldsymbol{\epsilon}) = (\mathbf{d}^\dagger + \delta\boldsymbol{\epsilon}^\dagger)\mathcal{C}(\mathbf{d}+\delta\boldsymbol{\epsilon})\\ - \lambda[(\mathbf{d}^\dagger + \delta\boldsymbol{\epsilon}^\dagger)(\mathbf{d}+\delta\boldsymbol{\epsilon}) - 1]\end{aligned} \tag{64}$$

where $\delta\boldsymbol{\epsilon}$ is a small vector perturbation on $\mathbf{d}$. Using the calculus of variations, the first variation of the functional is

$$\lim_{\delta\to 0}\frac{d}{d\delta}\mathcal{J}(\mathbf{d}+\delta\boldsymbol{\epsilon}) = \boldsymbol{\epsilon}^\dagger\,\mathcal{C}\,\mathbf{d} + \mathbf{d}^\dagger\,\mathcal{C}\,\boldsymbol{\epsilon} - \lambda(\boldsymbol{\epsilon}^\dagger\,\mathbf{d} + \mathbf{d}^\dagger\,\boldsymbol{\epsilon}), \tag{65a}$$

$$= \boldsymbol{\epsilon}^\dagger(\mathcal{C}\,\mathbf{d} - \lambda\,\mathbf{d}) + (\mathbf{d}^\dagger\,\mathcal{C}^\dagger - \lambda\,\mathbf{d}^\dagger)\boldsymbol{\epsilon}, \tag{65b}$$

$$= \boldsymbol{\epsilon}^\dagger(\mathcal{C}\,\mathbf{d} - \lambda\,\mathbf{d}) + [\boldsymbol{\epsilon}^\dagger(\mathcal{C}\,\mathbf{d} - \lambda\,\mathbf{d})]^\dagger. \tag{65c}$$

Therefore, finding the vectors that maximize their projection onto the data is equivalent to finding the eigenvalues λ_k and eigenvectors $\mathbf{d}_k$ of the covariance matrix:

$$\mathcal{C}\,\mathbf{d}_k = \mathbf{d}_k\,\lambda_k, \tag{66a}$$

or

$$\mathcal{C}\,\mathbf{D} = \mathbf{D}\,\boldsymbol{\Lambda}, \tag{66b}$$

where the columns of $\mathbf{D} = (\mathbf{d}_1, \mathbf{d}_2, \ldots, \mathbf{d}_{N_t})$ are the eigenvectors of $\mathcal{C}$ and $\boldsymbol{\Lambda}$ is a diagonal matrix of the eigenvalues in decreasing order. The covariance in Equation (63a) is a Hermitian $\mathcal{C} = \mathcal{C}^\dagger$ positive semi-definite matrix with non-negative eigenvalues that can be ordered by decreasing value $\lambda_1 \geqslant \lambda_2 \geqslant \ldots \geqslant \lambda_{N_t-1} \geqslant \lambda_{N_t} \geqslant 0$ with orthonormal eigenvectors[15]

$$\delta_{ij} = \mathbf{d}_i^\dagger\cdot\mathbf{d}_j, \tag{67a}$$

$$\delta_{ij} = \sum_{n=1}^{N_t}\mathbf{D}_{ni}^*\,\mathbf{D}_{nj}, \tag{67b}$$

$$\mathbf{I} = \mathbf{D}^\dagger\,\mathbf{D}, \tag{67c}$$

where $\mathbf{I}$ is the identity matrix. Assuming that the image sequence can be described by a $\mathbb{C}^{N_\mathrm{D}\times N_t}$ matrix of spatial eigenmodes $\boldsymbol{\Phi}$ and $\mathbb{C}^{N_t\times N_t}$ matrix of temporal coefficients $\boldsymbol{\alpha}$, this *ansatz* takes the form (as shown in Equation (32) repeated here for convenience)

$$\boldsymbol{I} = \boldsymbol{\Phi}\,\boldsymbol{\alpha}^\dagger,$$

where

$$\boldsymbol{\alpha} \equiv \mathbf{D}\,\boldsymbol{\Lambda}^{1/2}. \tag{68}$$

Post-multiplying Equation (32) by $\mathbf{D}$ and using the orthogonality relationship (67c)

$$\boldsymbol{I}\,\mathbf{D} = \boldsymbol{\Phi}\,\boldsymbol{\Lambda}^{1/2} \tag{69}$$

results in the equation for the spatial eigenfunctions $\boldsymbol{\Phi}$, where

$$\boldsymbol{\Phi} \equiv \boldsymbol{I}\,\mathbf{D}\,\boldsymbol{\Lambda}^{-1/2}. \tag{70}$$

Multiplying this by its adjoint

$$\boldsymbol{\Phi}^\dagger\,\boldsymbol{\Phi} = \boldsymbol{\Lambda}^{-1/2}\,\mathbf{D}^\dagger\,\boldsymbol{I}^\dagger\,\boldsymbol{I}\,\mathbf{D}\,\boldsymbol{\Lambda}^{-1/2}, \tag{71}$$

and using Equation (63a)

$$\boldsymbol{\Phi}^\dagger\,\boldsymbol{\Phi} = N_\mathrm{D}\,\boldsymbol{\Lambda}^{-1/2}\,\mathbf{D}^\dagger\,\mathcal{C}\,\mathbf{D}\,\boldsymbol{\Lambda}^{-1/2}, \tag{72}$$

followed by Equation (66b), produces

$$\boldsymbol{\Phi}^\dagger\,\boldsymbol{\Phi} = N_\mathrm{D}\,\boldsymbol{\Lambda}^{-1/2}\,\mathbf{D}^\dagger\,\mathbf{D}\,\boldsymbol{\Lambda}\,\boldsymbol{\Lambda}^{-1/2}, \tag{73}$$

which by virtue of Equation (67c) becomes the orthogonality relationship for the spatial eigenfunctions

$$\boldsymbol{\Phi}^\dagger\,\boldsymbol{\Phi} = N_\mathrm{D}\,\boldsymbol{\Lambda}^{-1/2}\,\boldsymbol{\Lambda}\,\boldsymbol{\Lambda}^{-1/2} = N_\mathrm{D}\,\mathbf{I}. \tag{74}$$

The temporal coefficients are orthogonal,

$$\boldsymbol{\alpha}^\dagger\,\boldsymbol{\alpha} = \boldsymbol{\Lambda}, \tag{75}$$

which implies that the temporal dynamics of the spatial eigenfunctions is on average uncorrelated. The temporal coefficients may also be used to reconstruct the covariance matrix

$$\mathcal{C} = \boldsymbol{\alpha}\,\boldsymbol{\alpha}^\dagger. \tag{76}$$

An analogous methodology could be applied to the two-point time-averaged spatial correlation function $\boldsymbol{I}\boldsymbol{I}^\dagger/N_t$ instead of the spatially averaged correlation function in Equation (63a). However, this direct method leads to a $\mathbb{C}^{N_\mathrm{D}\times N_\mathrm{D}}$ correlation matrix with $N_\mathrm{D} \simeq 10^7$ spatial eigenvalues and eigenvectors, which is prohibitively large for present computers. The method of snapshots, described above, is a practical method to obtain similar results when $N_t \ll N_\mathrm{D}$ (Sirovich 1987).

[15] Since the temporal median of each pixel is subtracted from the image sequence, the last eigenvalue λ_{N_t} will often be close to zero. Precision errors can manifest themselves as negative eigenvalues despite the positive semi-definite properties of the matrix $\mathcal{C}$. Standard practice is to set this negative eigenvalue to zero, effectively ignoring it in any modal reconstruction.

REFERENCES

Beck, J. G., & Giles, P. 2005, ApJL, 621, L153
Beckers, J. M., & Nelson, G. D. 1978, SoPh, 58, 243
Bjerhammar, A. 1951, Application of Calculus of Matrices to Method of Least Squares with Special Reference to Geodetic Calculations, Kungl. tekniska högskolans handlingar (Lindståhl)
Borrero, J. M., Tomczyk, S., Kubo, M., et al. 2011, SoPh, 273, 267
Cavanaugh, J. E. 1999, Statist. Probab. Lett., 42, 333
Centeno, R., Schou, J., Hayashi, K., et al. 2014, SoPh, 289, 3531
Chintzoglou, G., & Zhang, J. 2013, ApJL, 764, L3

Couvidat, S. 2014, in Solar Subsurface Flows from Helioseismology: Problems and Prospects, Helioseismology Workshop (Stanford, CA) http://hmi.stanford.edu/mtgs/workshop1407/agenda.html
Couvidat, S., Rajaguru, S., Wachter, R., et al. 2012, SoPh, 278, 217
Craven, P., & Wahba, G. 1979, NuMat, 31, 377
De Rosa, M. L., Schrijver, C. J., Barnes, G., et al. 2009, ApJ, 696, 1780
Emilio, M., Couvidat, S., Bush, R. I., Kuhn, J. R., & Scholl, I. F. 2015, ApJ, 798, 48
Garfinkel, B. 1964, AJ, 69, 567
Hathaway, D. 1988, SoPh, 117, 329
Hathaway, D. H. 1992, SoPh, 137, 15
Hathaway, D. H. 1996, ApJ, 460, 1027
Hathaway, D. H., & Rightmire, L. 2010, Sci, 327, 1350
Hoeksema, J. T., Liu, Y., Hayashi, K., et al. 2014, SoPh, 289, 3483
Högbom, J. A. 1974, A&AS, 15, 417
Holmes, P., Lumley, J. L., & Berkooz, G. 1996, Turbulence, Coherent Structures, Dynamical Systems and Symmetry (Cambridge: Cambridge Univ. Press)
Kazachenko, M. D., Fisher, G. H., Welsch, B. T., Liu, Y., & Sun, X. 2015, ApJ, 811, 16
LaBonte, B. J., Mickey, D. L., & Leka, K. D. 1999, SoPh, 189, 1
Leka, K. D. 2011, in ASP Conf. Ser. 437, Effects of Limited Resolution on SpectroPolarimetric data, from the Subtle to the Supreme, ed. J. R. Kuhn et al. (San Francisco, CA: ASP), 157
Leka, K. D., & Barnes, G. 2012, SoPh, 277, 89
Leka, K. D., Barnes, G., Crouch, A. D., et al. 2009, SoPh, 260, 83
Liu, Y., Hoeksema, J. T., Scherrer, P. H., et al. 2012, SoPh, 279, 295
Liu, Y., & Schuck, P. W. 2012, ApJ, 761, 105
Loéve, M. M. 1955, Probability Theory (Princeton, NJ: VanNostrand)
Lumley, J. L. 1967, in Atmospheric Turbulence and Wave Propagation, ed. A. M. Yaglom, & V. I. Tatarski (Moscow: Nauka)
Mochizuki, E. 1992, SoPh, 142, 395
Moore, E. H. 1920, BAMaS, 26, 394 http://projecteuclid.org/euclid.bams/1183425340
Orozco Suárez, D., Bellot Rubio, L. R., Del Toro Iniesta, J. C., et al. 2007, PASJ, 59, 837
Penrose, R. 1955, MPCPS, 51, 406 http://journals.cambridge.org/article_S0305004100030401
Peter, H., Warnecke, J., Chitta, L. P., & Cameron, R. H. 2015, A&A, 584, A68
Roberts, D. H., Lehar, J., & Dreher, J. W. 1987, AJ, 93, 968
Scherrer, P. H., Schou, J., Bush, R. I., et al. 2012, SoPh, 275, 207
Schou, J., Scherrer, P. H., Bush, R. I., et al. 2012, SoPh, 275, 229
Schuck, P. W. 2005, ApJ, 632, 53
Schuck, P. W. 2006, ApJ, 646, 1358
Schuck, P. W. 2008, ApJ, 683, 1134
Schuck, P. W. 2010, ApJ, 714, 68
Schwarz, G. 1978, AnSta, 6, 461
Sirovich, L. 1987, QApMa, XLV, 561
Smart, W. M. 1977, in Textbook on Spherical Geometry, ed. R. M. Green (6th ed.; New York: Cambridge Univ. Press), 174
Snodgrass, H. B. 1984, SoPh, 94, 13
Tange, O. 2011, login: The USENIX Magazine, 36, 42 http://www.gnu.org/s/parallel
Thompson, W. T. 2006, A&A, 449, 791
Vemareddy, P. 2015, ApJ, 806, 245
Wahba, G. 1980, Ill-posed Problems: Numerical and Statistical Methods for Mildly, Moderately and Severely Ill-posed Problems with Noisy Data, Tech. Rep. 595 (Madison, WI: Department of Statistics, Univ. Wisconsin)
Wang, H., Varsik, J., Zirin, H., et al. 1992, SoPh, 142, 11
Woltring, H. J. 1986, Advances in Engineering Software and Workstations, 8, 104
Ye, M., Meyer, P. D., & Neuman, S. P. 2008, WRR, 44